A Neural Network Classification Framework for Monthly and High Spatial Resolution Surface Water Mapping in the Qinghai–Tibet Plateau from Landsat Observations

Qinwei Ran, Filipe Aires, Philippe Ciais, Chunjing Qiu, Yanfen Wang

▶ **To cite this version:**

Qinwei Ran, Filipe Aires, Philippe Ciais, Chunjing Qiu, Yanfen Wang. A Neural Network Classification Framework for Monthly and High Spatial Resolution Surface Water Mapping in the Qinghai–Tibet Plateau from Landsat Observations. Journal of Hydrometeorology, 2023, 24 (10), pp.1635-1657. 10.1175/JHM-D-22-0211.1 . hal-04330615

HAL Id: hal-04330615
https://hal.science/hal-04330615v1

Submitted on 16 Jan 2025

HAL is a multi-disciplinary open access archive for the deposit and dissemination of scientific research documents, whether they are published or not. The documents may come from teaching and research institutions in France or abroad, or from public or private research centers.

L'archive ouverte pluridisciplinaire **HAL**, est destinée au dépôt et à la diffusion de documents scientifiques de niveau recherche, publiés ou non, émanant des établissements d'enseignement et de recherche français ou étrangers, des laboratoires publics ou privés.

Distributed under a Creative Commons Attribution 4.0 International License

A Neural Network Classification Framework for Monthly and High Spatial Resolution Surface Water Mapping in the Qinghai–Tibet Plateau from Landsat Observations

QINWEI RAN,[a,b,c] FILIPE AIRES,[b] PHILIPPE CIAIS,[c] CHUNJING QIU,[c] AND YANFEN WANG[d,e,f]

[a] *College of Life Sciences, University of Chinese Academy of Sciences, Beijing, China*
[b] *Laboratoire d'Études du Rayonnement et de la Matière en Astrophysique et Atmosphères, Observatoire de Paris, Paris, France*
[c] *Laboratoire des Sciences du Climat et de l'Environnement, CEA CNRS UVSQ, Gif sur Yvette, France*
[d] *College of Resources and Environment, University of Chinese Academy of Sciences, Beijing, China*
[e] *Beijing Yanshan Earth Critical Zone National Research Station, University of Chinese Academy of Sciences, Beijing, China*
[f] *State Key Laboratory of Tibetan Plateau Earth System Science (LATPES), Beijing, China*

(Manuscript received 22 November 2022, in final form 13 June 2023, accepted 17 July 2023)

ABSTRACT: The Qinghai–Tibet Plateau, known as the Asian Water Tower, has a significant area of water bodies that provide a wide range of valuable ecosystem services. In the context of climate change, the formation condition of surface water and water extent is changing fast. Thus, there is a critical need for monthly detection algorithms at high spatial resolution (~30 m) with good accuracy. Multiple sensors' observations are available, but producing reliable long time series surface water mapping at a subannual temporal frequency still remains a challenge, mainly due to data limitations. In this study, we proposed a neural-network-based monthly surface water classification framework relying on *Landsat 5/7/8* images in 2000–20 and topographic indices, and retrieved monthly water mask for the year 2020. The surface water was mainly distributed in the central and western parts of the plateau and the maximum area of permanent surface water (water frequency > 60%) was 26.66×10^3 km^2 in 2020. The overall, producer, and user accuracies of our surface water map were 0.96, 0.94, and 0.98, respectively, and the kappa coefficient reached 0.90, demonstrating a better performance than existing products [i.e., Joint Research Centre (JRC) Monthly Water History with overall accuracy 0.94, producer accuracy 0.89, user accuracy 0.99, and kappa coefficient 0.89]. Our framework efficiently solved the problem of missing data in Landsat images referring to the JRC and a priori information and performed well in dealing with ice/snow cover issues. We showed that higher uncertainties exist on wetlands and recommended exploring relationships between water and wetlands in the future.

SIGNIFICANCE STATEMENT: In this paper, we present a new methodology to estimate surface water and its intra-annual changes using Landsat data. Missing data and retrieval errors in the winter are major issues in the existing products (i.e., JRC dataset). This motivated us to develop a new machine learning algorithm to better improve the retrieval scheme. We show that our approach, based on a neural network classifier, delivers a significant improvement compared to the previous estimates. As shown in the literature, JRC data can hardly be used at the monthly level, whereas our retrieval appears to be exploitable at the monthly scale. This is essential to understand the trend in surface water, one of the key elements of the water cycle.

KEYWORDS: Water resources; Remote sensing; Satellite observations; Classification

1. Introduction

Known as the "Asian Water Tower," the Qinghai–Tibet Plateau has numerous lakes and is the source of many rivers providing precious water resources for human needs (Qu et al. 2019). On the one hand, the formation of water might be changing over a period, e.g., rainfall or snowmelt. Furthermore, the widely distributed glaciers and permafrost in this region have been influenced by climate change and the hydrological cycle appears to have been intensified, resulting in significant area changes of surface water (Yang et al. 2014). The "water goal" set in the United Nations' Sustainable Development Goals (SDGs) 6 for sustainable water management gives a strong impetus for continuously monitoring monthly surface water with high spatial resolution.

Previous studies on surface water mapping with 30-m spatial resolution (Table 1) have provided us with unprecedented information for understanding surface water dynamics. Yet, most of these studies extract water information based on one or more years of composite images, instead of benefiting from the whole time series (Zhang et al. 2014; Chen et al. 2017; Gong et al. 2013; Feng et al. 2016). Gong et al. (2013) collected Landsat images from 1984 to 2011 and obtained a global land cover mapping based on synthetic images. They provided a one-time static surface water extent, which does not allow for the monitoring of recent dynamics. We also note that the surface area in the Qinghai–Tibet Plateau was quite different among these studies, ranging from 50×10^3 to 100×10^3 km^2 (Zhang et al. 2014; Chen et al. 2017; Gong et al. 2013; Feng et al. 2016; Wang et al. 2020; Pekel et al. 2016; Ran et al. 2023; Pickens et al. 2020). The studies that generated annual water body products are from Wang et al. (2020), who proposed yearly surface water maps across all China from 1989 to 2016,

Corresponding authors: Filipe Aires, filipe.aires@obspm.fr; Yanfen Wang, yfwang@ucas.ac.cn

DOI: 10.1175/JHM-D-22-0211.1

© 2023 American Meteorological Society. This published article is licensed under the terms of the default AMS reuse license. For information regarding reuse of this content and general copyright information, consult the AMS Copyright Policy (www.ametsoc.org/PUBSReuseLicenses).

Unauthenticated | Downloaded 01/16/25 10:26 AM UTC

TABLE 1. Surface water mapping datasets covering the Qinghai–Tibet Plateau at 30-m spatial resolution.

Datasets	Temporal resolution	Surface water area (km^2)	Period	Satellite data	Method	Reference
Chinacover	Composite	61×10^3	2010 composite	Chinese Huan Jing (HJ) satellite	Object-based hierarchical classification	Zhang et al. (2014)
Globeland 30	Composite	51×10^3	2009–11 (80%) composite	Landsat TM and ETM+, HJ-1	Combining MLC, SVM, threshold method	Chen et al. (2017)
FROM-GLC 30	Composite	101×10^3	1984–2011 composite	Landsat TM and ETM+	Conventional maximum likelihood, J4.8 decision tree, random forest, support vector machine	Gong et al. (2013)
GLCF GIW	Composite	—	1999–2000 composite	Landsat ETM+	Classification-tree mode; water and vegetation indices (NDVI, NDWI, MNDWI), terrain indices (slope, hill-shade)	Feng et al. (2016)
—	Yearly	—	1989–2016	Landsat TM, ETM+, and OLI	mNDWI-VIs algorithm	Wang et al. (2020)
JRC Monthly Water History	Monthly (with many missing data)	69×10^3 (in 2019)	1984–2020	Landsat TM, ETM+, and OLI	Expert systems, visual analytics and evidential reasoning	Pekel et al. (2016)
—	Yearly	63×10^3 (in 2020)	2000–20	Landsat TM, ETM+, and OLI	Random forest	Ran et al. (2023)
GLAD	Monthly (with many missing data)	82×10^3 (in 2020)	1999–2021	Landsat TM, ETM+, and OLI	Classification trees	Pickens et al. (2020)

Unauthenticated | Downloaded 01/16/25 10:26 AM UTC

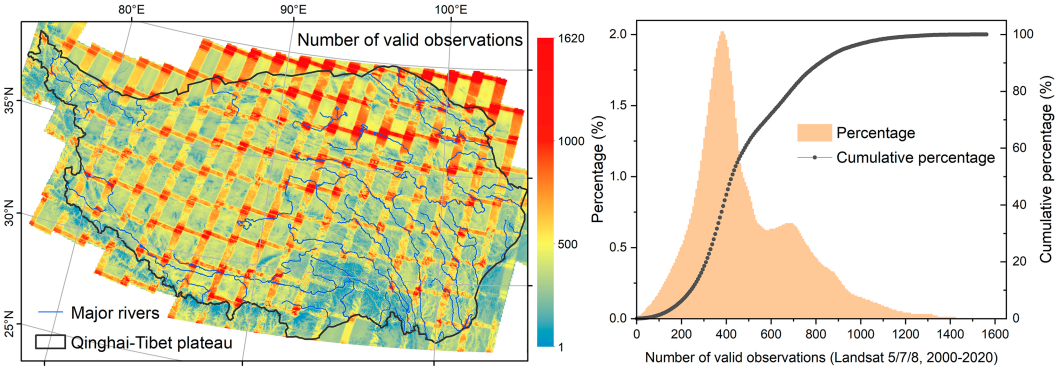

FIG. 1. (left) Number of valid Landsat observations after cloud-filtering (*Landsat 5/7/8* fusion) over the 2000–20 period. (right) Histogram and cumulative percentage of the number of valid observations for all the pixels of the domain for the whole period.

and Ran et al. (2023), who derived yearly surface water maps in the Qinghai–Tibet Plateau from 2000 to 2020. However, these studies do not give insights on the monthly dynamics of surface water. The European Commission Joint Research Centre (JRC) Monthly Water History dataset (Pekel et al. 2016) and global surface water dynamics (Pickens et al. 2020) give updated monthly extent of surface water, which are currently the long time series monthly classification dataset at 30-m resolution with open access at the global scale, and by far the most widely used global surface water dataset. However, these datasets are restricted by the missing data of Landsat observations (Meyer et al. 2020; Pickens et al. 2020), and therefore monthly estimates can hardly be fully used. Moreover, the time series of the JRC dataset are shown to miss fluctuations caused by climate events (Wang et al. 2020).

Mapping surface water from satellites is constrained by the spatial/temporal resolution and geographic/time scope. Studies have revealed that there is a trade-off between the temporal and spatial resolutions of the satellite sensors, with current noncommercial satellites offering either high temporal resolution images with coarse spatial resolution, or high spatial resolution images with sparse temporal resolution (Li et al. 2021; Zhu et al. 2018). The Moderate Resolution Imaging Spectroradiometer (MODIS) provides daily images and has the advantage of detecting temporal dynamics, with few studies giving surface water dataset at an 8-day time step (Li et al. 2021; Lu et al. 2017). However, the spatial resolution (i.e., 250 m) is too coarse to capture subtle changes in small water bodies. *Sentinel-2* Multispectral Instrument (MSI) was launched in 2015, with a spatial resolution of 10 m and revisit cycle of 10 days, and is one of the data sources for refined surface water mapping (Kordelas et al. 2018; Wang et al. 2018). The WorldCover product was generated based on *Sentinel-1* and *Sentinel-2* data, which is a global land cover map (including surface water extent) for 2020 at 10-m resolution (Zanaga et al. 2021). The big size and archive accessibility make Sentinel data heavy to process and the length of the data archive does now allow to reconstruct long time series. Landsat [Thematic Mapper (TM), Enhanced Thematic Mapper Plus (ETM+), and Operational Land Imager (OLI)] has been a widely used data source for large-scale, refined, dynamic surface water mapping studies. Since the first sensor launched in 1972, Landsat has provided continuous Earth observations for almost 50 years, which makes it possible for long time series analysis (Bullock et al. 2020; Zhu 2017). In addition, Landsat data are adequate to detect water body types (lakes, rivers, ponds, etc.) and also monthly and seasonal variations (Chen et al. 2020; Senay et al. 2017; Halabisky et al. 2016) with high spatial (30 m) and temporal (16 day) resolutions. With the rapid development of the Google Earth Engine (GEE) platform, the open access to the Landsat archive makes the processing more convenient and efficient (Gorelick et al. 2017; Tamiminia et al. 2020). However, due to cloud contamination and instrumental defects, missing observations may result in uncertainties when using such Landsat images (Wang et al. 2012; Zhang et al. 2017). Therefore, more efforts should be put into image preprocessing to improve the spatial continuity and quality, especially for large-scale studies.

There are many methodologies for surface water mapping. Spectral-index-based threshold method, decision tree, expert system, and machine learning are commonly used for supervised classification. The spectral-index-based threshold is a convenient and efficient method to extract surface water information, it is linked to the spectral distribution characteristics of the different land cover types. Water indices and vegetation indices are the commonly used spectral indexes for surface water classification (Feyisa et al. 2014; Xu 2006; Qiao et al. 2012; Wang et al. 2020; Fisher et al. 2016). Using the modified normalized difference water index (mNDWI), enhanced vegetation index (EVI), and normalized difference vegetation index (NDVI), Zou et al. (2017) and Wang et al. (2020) proposed the mNDWI-VIs algorithm and reported long-time series of annual surface water maps in China and Oklahoma, respectively. However, the spectral-index-based threshold method is not universal especially in large-scale studies, because the classification criteria is based on a limited number of samples, and the threshold varies with time and location (Feyisa et al. 2014). The expert system is another commonly used method. It integrates diverse models and exploits multiple data sources to generate expert rules (Pekel et al. 2016; Gumbricht et al. 2017). Pekel et al. (2016) adopted such

Unauthenticated | Downloaded 01/16/25 10:26 AM UTC

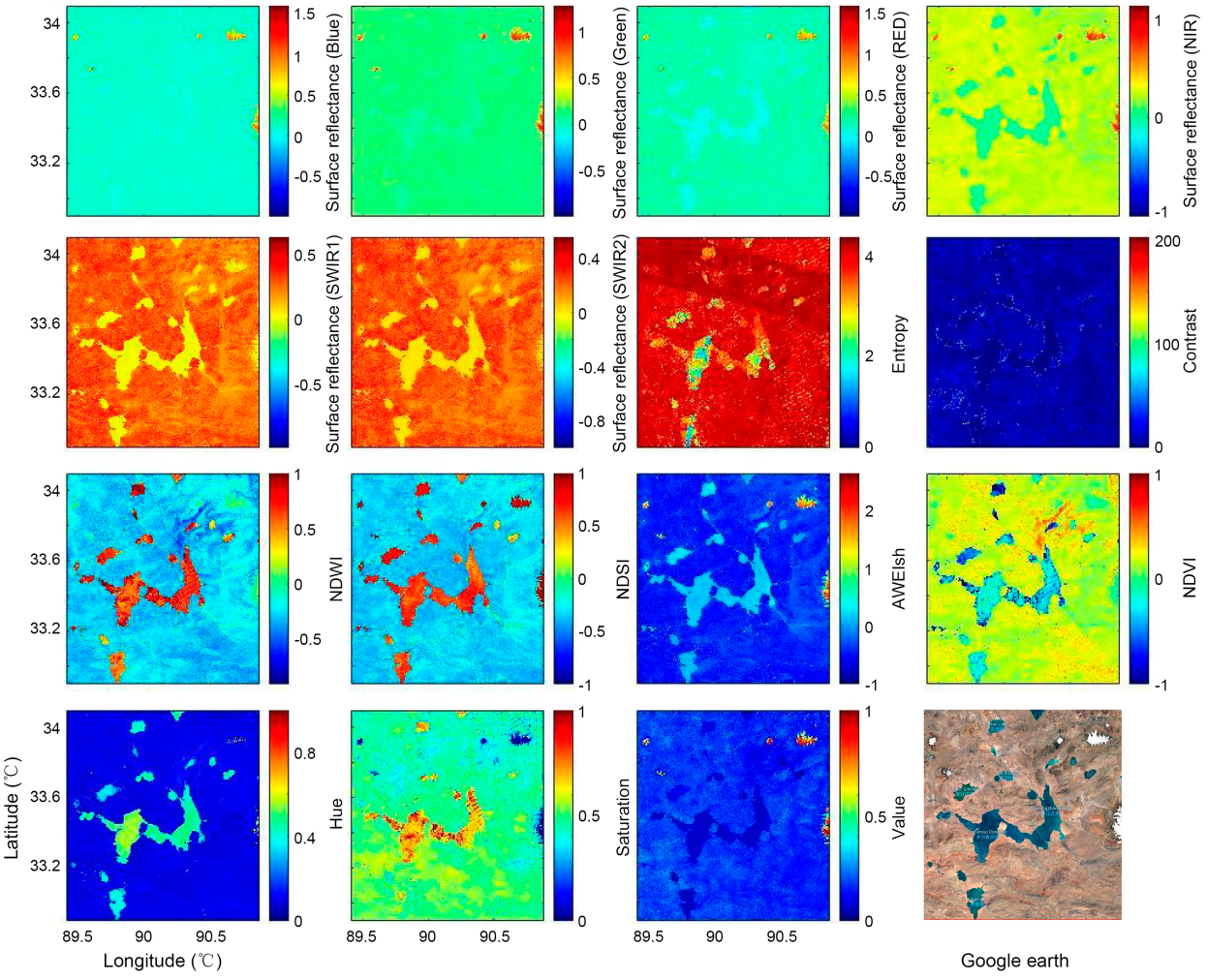

FIG. 2. Examples of Landsat spectral features (see Table 2) in the small region of the Qinghai–Tibet Plateau at 30-m spatial resolution (August 2020), including blue, green, red near-infrared (NIR), shortwave infrared 1 (SWIR1), and SWIR2 surface reflectance bands; entropy and contrast texture attributes; NDWI, NDSI, AWEIsh, and NDVI spectral indexes; hue, saturation, and value color features (Table 2).

an expert system method using the Landsat archive as well as a series of auxiliary datasets [digital elevation model (DEM), lava mask, glacier data, etc.] to obtain a long-term water record. The expert system method is flexible and can easily be adjusted by experts, but it is highly affected by the data source and model (Gumbricht et al. 2017; Stefanov et al. 2001). Machine learning classification methods, such as decision tree (Pal and Mather 2003; Wu et al. 2021), random forest (Ghorbanian et al. 2020), extreme gradient boosting (XGBoost; Georganos et al. 2018), and neural network (NN) classifier (Aires et al. 2021; Scott et al. 2017), have become popular in the land-cover community. Among these machine learning methods, NN classifier is thought to be robust and tolerant, and adequate to deal with complex problems (Aires et al. 2021; Kulkarni and Lowe 2016). Jiang et al. (2018) adopted a multilayer perceptron NN for surface water classification with a higher performance, compared to the water index method or the support vector machine algorithm. Rezaee et al. (2018) proposed a convolutional NN-based framework for completing complex wetland classification and their result showed better performance than random forest even when using a small number of input features. It is actually shown that if there are enough samples and hidden neurons, any complex relationship can be represented by a neural network (Cybenko 1989). However, the performance of NN retrieval greatly relies on the size and quality of the reference database (Aires et al. 2021).

Here, we propose a NN-based monthly surface water classification framework using the 30-m Landsat data and some topographic indexes. Our method has several improvements compared with previous studies:

1) We developed some solutions for the problem of invalid observations (e.g., missing or negative data), at a finer temporal resolution, which greatly improved the accuracy of the classification results.

Unauthenticated | Downloaded 01/16/25 10:26 AM UTC

TABLE 2. Summary of spectral features.

No.	Input	Description
1	Blue	Surface reflectances
2	Green	
3	Red	
4	NIR	
5	SWIR1	
6	SWIR2	
7	Entropy	Texture attribute measuring the randomness of a gray-level distribution
8	Contrast	Texture attribute measuring the local contrast of an image
9	NDWI	Normalized difference water index
10	NDSI	Normalized difference snow index
11	AWEIsh	Automated water extraction index shadow
12	NDVI	Normalized difference vegetation index
13	Hue	Color model related to a full saturation
14	Saturation	Color model related to the purity and intensity of the color
15	Value	Color model related to relative lightness or darkness of the color

2) We conducted a preliminary filtering that greatly reduced the amount of data and the computation cost.
3) The NN method provides its prediction results with a probability value for the presence of surface water instead of a binary value, which enables us to propose a quality flag index to assess the pixel classification reliability.
4) We used seasonal models that are stable and robust for the monthly surface water mapping.
5) We collected hundreds of field samples, especially river samples, and unmanned aerial vehicle (UAV) images, that can be used to better evaluate the mapping result.

This paper is structured as follows. The datasets are presented in section 2: specifically, the adopted strategies to deal with invalid pixels and to generate monthly Landsat composites are introduced in sections 2a and 2b, respectively, and the inputs for the classification (i.e., the spectral information and topography-based indices) are proposed in section 2c. Section 2d introduces field investigation samples, UAV images, and the European Space Agency (ESA) WorldCover dataset, that are used as reference data for evaluation. The detailed classification algorithm is described in section 3. Then, we evaluate the surface water mapping performance in the year 2020 by comparing it with the reference datasets (section 4a), and analyze the monthly patterns (section 4b). Finally, we summarize our results and provide perspectives in section 5.

2. Data

a. *Landsat dataset*

All available *Landsat 5*/*7*/*8* Collection 2 surface reflectance images from 2000 to 2020 were utilized here. This is the latest version released by the United States Geological Survey (USGS) in 2020 with more advanced data processing algorithm. Landsat images before 2000 were confirmed to have a larger proportion of wrong observation pixels (Wang et al. 2020). More high-quality images can be obtained after the launch of *Landsat 7* and *Landsat 8* in 1999 and 2013, respectively, making it possible to detect surface water since 2000 with higher precision, and at the monthly scale. Figure 1 shows the spatial distribution and histograms of valid observation numbers after filtering cloud and cloud shadow at pixel scale, over the study period between 2000 and 2020. About 90% of the individual pixels obtain more than 300 valid observations. The monthly pixels percentage and spatial distribution of Landsat data were displayed in Figs. A1 and A2, respectively. On average, more than 85% of pixels have one or more images per month.

b. *Image preprocessing*

The quality assurance (QA) variable was referred to identify the cloud-contaminated observations for each image. Then, to fill the data gaps preliminarily, images from different sensors were fused to generate monthly composites according to the median value. For the study of surface information extraction, clouds often lead to the weakening or even loss of land cover information (Shen et al. 2014). As shown in Fig. A1, invalid observations, including missing data and negative reflectance data, were present every month over the Qinghai–Tibet Plateau. Therefore, pixels with missing data were filled using a priori information, that is neighboring information based on a historical record (Aires 2020). Here, the monthly average value from 2000 to 2020 was used for data filling. For pixels with negative data over water, using the JRC dataset as a reference supplemented by visual interpretation, the pixel value was assigned to 0, while for those over land, the data were filled using a priori information. After these preprocessing steps, the average percentage of monthly valid pixels increased from 86.3% to 99.7% (Fig. A1), which ensured the spatial continuity of the classification results. Thus, data quality increased to a satisfying physical coherency.

Spectral features, such as water index, vegetation index, surface texture, and color information, were validated as effective for surface water extraction (Ran et al. 2023). These features were calculated on the time series of the image collection and were the potential predictors in the forthcoming classifier (Fig. 2, Table 2), including two texture attributes measured with a gray-level co-occurrence matrix (GLCM): entropy and contrast (Haralick et al. 1973; Conners et al. 1984); three water

Unauthenticated | Downloaded 01/16/25 10:26 AM UTC

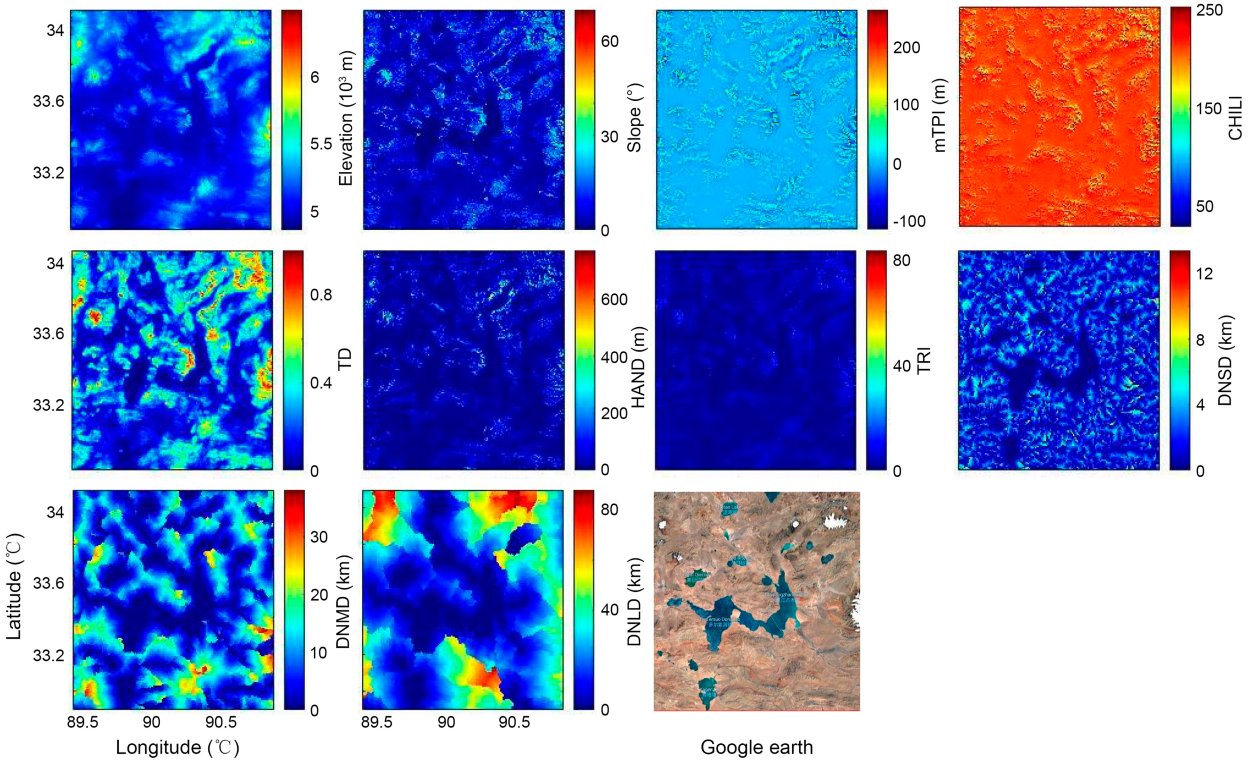

FIG. 3. Examples of topographic features in the Qinghai–Tibet Plateau retrieved from the SRTM DEM and the MERIT Hydro dataset, including elevation, slope, mTPI, CHILI, TD, HAND, TRI, DNSD, DNMD, and DNLD (Table 3).

indices: normalized difference water index (NDWI; Gao 1996); automated water extraction index shadow (AWEIsh; Feyisa et al. 2014), and normalized difference snow index (NDSI; Hall et al. 1995); one vegetation index: NDVI (Rouse et al. 1974); and three color attributes: hue, saturation, and, value (Wu et al. 2014). All Landsat image acquisition and processing tasks were conducted on GEE cloud platform.

c. *Topographic data*

Topographic information was used to facilitate surface water detection because hydrology is often influenced by elevation. Elevation affects factors such as slope, topography, and drainage patterns, which further influence hydrological processes (Aires et al. 2018). As shown in Fig. 3 and Table 3, elevation and slope were derived from the 30-m SRTM DEM dataset. The multiscale topographic position index (mTPI), continuous heat-insolation load index (CHILI), yopographic diversity (TD), and landforms were ecologically relevant layers of topographic information (Theobald et al. 2015). Height above the nearest drainage (HAND) was obtained from the MERIT (Multi-Error-Removed Improved-Terrain) Hydro dataset, which is a global flow direction dataset with a resolution of 3 arc-s (Yamazaki et al. 2019). The terrain ruggedness index (TRI) was calculated using a 30-m SRTM DEM dataset based on System for Automated Geoscientific Analyses (SAGA) GIS. The DNSD

TABLE 3. Summary of topographic features.

No.	Input	Spatial resolution (m)	Description
1	Elevation	30	—
2	Slope	30	—
3	mTPI	270	Multiscale topographic position index ranging from negative (valleys) to positive (ridges) values
4	CHILI	90	Continuous heat-insolation load index ranging from 0 (very cool) to 255 (very warm)
5	TD	270	Topographic diversity refers to the temperature and moisture conditions available to local species
6	HAND	90	Height above the nearest drainage
7	TRI	30	Terrain ruggedness index is a measure of local topographic relief
8	DNSD	90	Distance to the nearest small drainage with upstream area > 0.5 km^2
9	DNMD	90	Distance to the nearest medium drainage with upstream area > 10 km^2
10	DNLD	90	Distance to the nearest large drainage with upstream area > 100 km^2

Unauthenticated | Downloaded 01/16/25 10:26 AM UTC

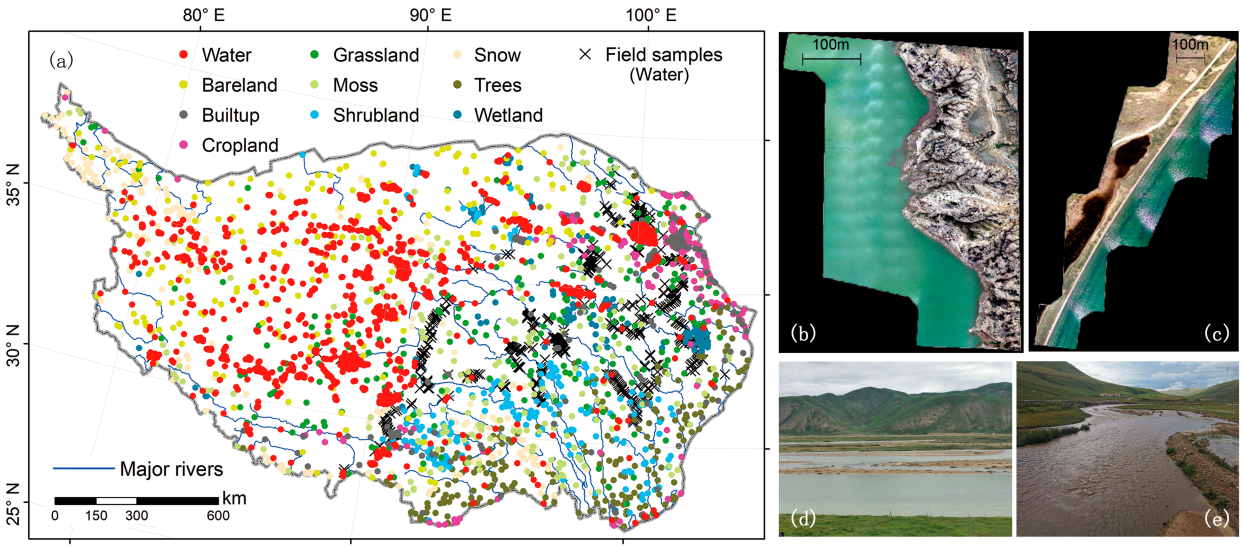

FIG. 4. (a) Location of the ESA WorldCover sampling points (1400 for surface water and 200 for each of the other land cover types) and the field investigation samples used for evaluation; (b),(c) examples of UAV images and (d),(e) field investigation pictures.

(distance to the nearest small drainage), DNMD (distance to the nearest medium drainage), and DNLD (distance to the nearest large drainage) represent the distances to the nearest drainage with an upstream area larger than 0.5, 10, and 100 km^2, respectively. These topographic inputs were downscaled to 30 m using the nearest-neighbor method.

d. Reference datasets for evaluation

1) ESA WORLD COVER SURFACE TYPE

The WorldCover product, released by ESA, provides a global land cover map with a resolution of 10 m for 2020 using *Sentinel-1* and *Sentinel-2* data (Zanaga et al. 2021). This

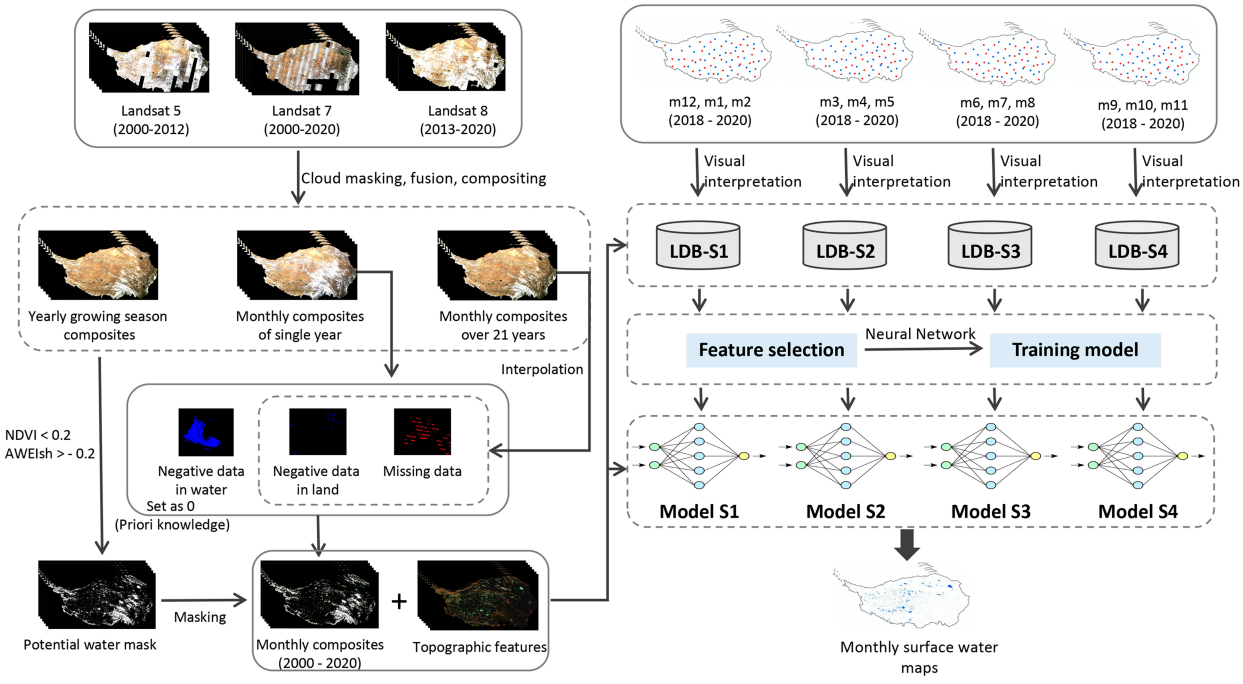

FIG. 5. Workflow for the monthly surface water mapping. m represents month: four seasonal training datasets were created using monthly samples from the same season, and then seasonal NN prediction models were developed. LDB represents learning database, including monthly spectral features and topographic features.

Unauthenticated | Downloaded 01/16/25 10:26 AM UTC

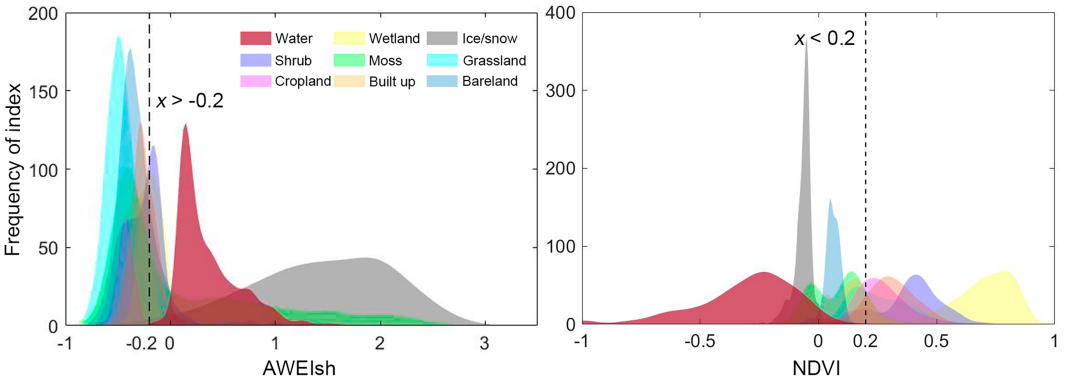

FIG. 6. AWEIsh and NDVI histograms for different land-cover types from the ESA WorldCover map. The nonwater pixels are masked using these two potential water thresholds (AWEIsh > -0.2 and NDVI < 0.2).

dataset includes 10 land cover types over the Qinghai–Tibet Plateau: water, bare land, built-up, cropland, grassland, moss, shrubland, snow, trees, and wetland. First, the WorldCover dataset was upscaled to 30 m and pixels containing mixed land-cover types were removed. Then, random sampling was conducted on each land-cover type for evaluation, including 1400 water samples, and 200 samples for each of the other nine land-cover types (Fig. 4a). Manual validation was finally performed to ensure the samples' quality.

2) GROUND DATA

Field surveys using a UAV equipped with DJI Phantom 4 pro platform were conducted in August 2020, taking a series of high-resolution multispectral images of Yellow River sources, Qinghai Lake, Longyang Gorge, and Star Lake of the Qinghai–Tibet Plateau to detect the boundary of typical lakes (Jia et al. 2021). The flight was implemented under good weather conditions, and the route was planned to be centered on the water–land boundary of lakes. Figures 4b and 4c are examples of true-color drone images at 5-cm resolution.

We conducted field surveys along rivers during the growing season of 2020/21, considering the difficulties in river mapping. 930 sampling points were marked as water in total. Meanwhile, digital cameras were used to take pictures of the scene and global positioning system (GPS) was used to record the location. We recorded the morphological characteristics of the river (river width, river depth, and river turbidity) and the characteristics of the environment (human disturbance, and riparian vegetation). These sampling points were uploaded to GEE to facilitate the correction through visual

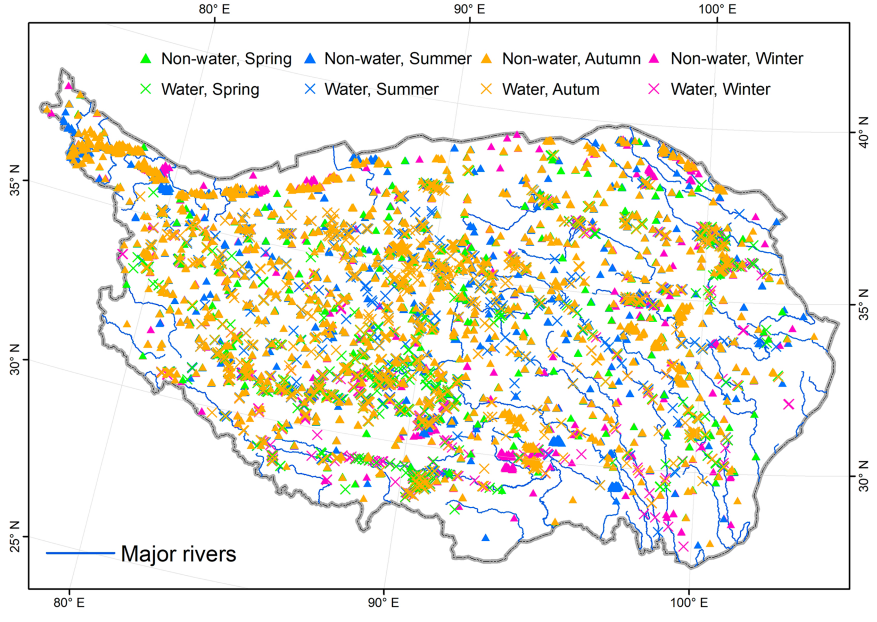

FIG. 7. Spatial distribution of training dataset. Green, blue, orange, and purple represent samples from spring, summer, autumn, and winter months, respectively. Triangles and crosses represent nonwater and water samples, respectively.

Unauthenticated | Downloaded 01/16/25 10:26 AM UTC

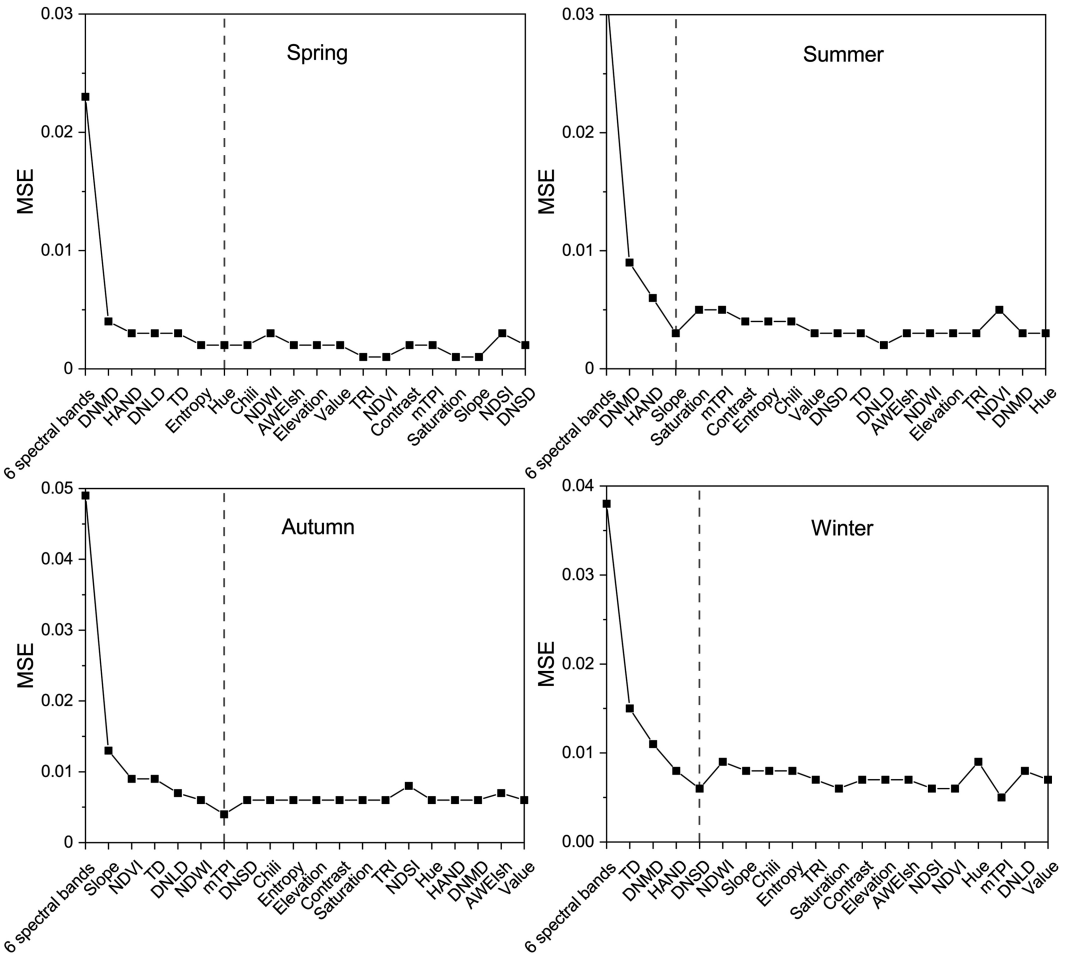

FIG. 8. Step-forward feature selection for the four seasonal models. The *y* axis represents the MSE for the model's predictions using the current feature combined with the previously selected features. The dashed line indicates the last selected factor, which, along with the previous features, serves as input to the model.

interpretation. Sampling points distributed in small rivers were deleted (i.e., river width less than 30 m). Finally, 471 samples were reserved and used for evaluation. Figure 4a shows the spatial distribution and some examples of field pictures recorded during this ground survey.

3. Methods

a. Overview of the classification algorithm

Our monthly water classification model includes two main parts: Landsat time series preparation (sections 3b and 3c) and the original water classification scheme (section 3d). In the first part, after the preprocessing of Landsat images, spatially continuous monthly images in a single year were obtained by calculating the average value first and filling missing data with a priori information (neighboring information based on a historical record). The annual potential water extent was then generated using spectral indices thresholds based on the Landsat annual composites. Thereafter, monthly images were prepared by combining spatially continuous monthly images with the annual potential water extent map, to facilitate the forthcoming NN classification. In the second part, monthly classification was achieved through building the learning database (monthly spectral features and topographic features), training seasonal models, and then performing pixel-by-pixel prediction. The workflow of monthly surface water classification is shown in Fig. 5.

b. Potential water filtering

To reduce data size and computation cost, and thus improve the classification efficiency in a large-scale study, we developed a preliminary potential water extent mask by excluding nonwater areas. Figure 6 shows the AWEIsh and NDVI histograms of different land-cover types in the Qinghai–Tibet Plateau. The index values were extracted from the 2020 composite images, and the average value was calculated for each land-cover type. We can see that there was a fair separation between water (red) and the other land-cover types when considering both conservative thresholds of AWEIsh > -0.2 and NDVI < 0.2. These thresholds suppressed unambiguous nonwater pixels. We

Unauthenticated | Downloaded 01/16/25 10:26 AM UTC

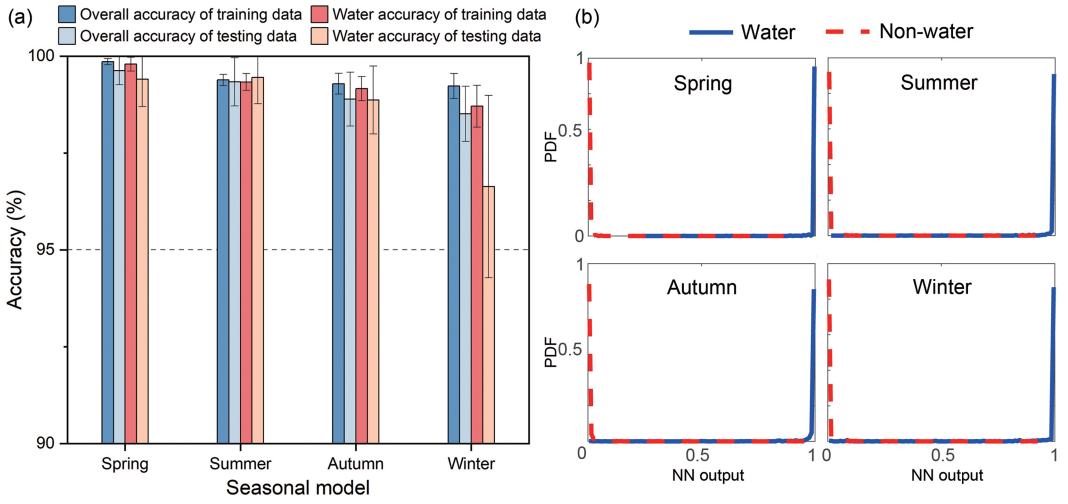

FIG. 9. (a) Classification performance of the ninefold cross-validation assessment of the four seasonal models. The results of the nine classifications were averaged by season to estimate the seasonal mean water accuracy and overall accuracy. (b) Probability density function (PDF) of the NN classifier outputs for the four seasonal models, for the water (blue) and the land (dotted red) pixels, over the testing database.

conservatively kept in our mask some cases of ambiguous water (located in mountains and rivers) and nonwater situations, because it will be the role of the forthcoming classification to disentangle these nonwater pixels.

c. *Neural network classification*

1) BUILDING THE LEARNING DATABASE

The learning database was built using a stratified random sampling strategy. First, monthly samples (30 m × 30 m pixel) were collected in 2018–20. For each month, 100 water samples and 100 nonwater samples based on the JRC dataset were randomly selected. Then, all samplings were checked and relabeled with visual interpretation based on high-resolution images. Therefore, a collection of 7200 (200 samples × 12 months × 3 years) samples were obtained. In addition, samples in difficult and ambiguous regions were collected through visual interpretation. After extracting the values of input features (15 spectral and 10 topographic features in Tables 2 and 3), four learning databases were built by gathering samples in the following seasons: S1 (December–February), S2 (March–May), S3 (June–August), and S4 (September–November) (Fig. 7) (Xu et al. 2019; Shen 2011; Zhang et al. 2021).

2) NEURAL NETWORK CLASSIFIER

NN has been widely used for surface information extraction (Aires and Pellet 2021; Ienco et al. 2017). Our study used seasonal NN classifiers to identify water or nonwater pixels. A NN is defined first by an architecture. The inputs (from 6 to 25 depending on the seasonal model) represent the input layer. The experiments and iterative improvements showed that having 10 neurons in the hidden layer achieves a balance between model complexity and flexibility and a unique hidden layer is sufficient for water body extraction. Then, the unique hidden layer of 10 neurons connected to one output neuron

TABLE 4. Error matrix of our results and JRC dataset. The reference dataset is based on field samples, visual interpretation, and ESA world cover dataset, for August 2020. Note: P_Accuracy is the producer accuracy, U_Accuracy is the user accuracy, and kappa is the kappa coefficient.

		Reference data				
	Class	Nonwater	Water	Total	U_accuracy	kappa
Our result (Aug 2020)	Nonwater	1771	116	1887	0.94	—
	Water	29	1665	1694	0.98	—
	Total	1800	1781	3581	—	—
	P_Accuracy	0.98	0.94	—	0.96	—
	kappa	—	—	—	—	0.90
JRC (Aug 2020)	Nonwater	1798	197	1995	0.90	—
	Water	2	1584	1586	0.99	—
	Total	1800	1781	3581	—	—
	P_Accuracy	0.99	0.89	—	0.94	—
	kappa	—	—	—	—	0.88

Unauthenticated | Downloaded 01/16/25 10:26 AM UTC

TABLE 5. Classification accuracy of all land cover types of our results and JRC dataset. The reference dataset is based on field samples, visual interpretation, and ESA world cover dataset, for August 2020.

		Reference data										
		Water	Nonwater	Trees	Shrub land	Grassland	Cropland	Built-up	Barren	Snow/ice	Herbaceous wetland	Moss and lichen
		Field samples and ESA WorldCover					ESA WorldCover					
Our result (Aug 2020)	Water	1665	29	0	0	0	0	0	0	1	1	27
	Nonwater	116	1771	200	200	200	200	200	200	199	199	173
	Accuracy	0.94	0.98	1	1	1	1	1	1	0.99	0.99	0.88
JRC (Aug 2020)	Water	1584	2	0	0	0	0	0	1	0	0	1
	Nonwater	197	1798	200	200	200	200	200	199	200	200	199
	Accuracy	0.90	0.99	1	1	1	1	1	0.99	1	1	0.99

representing the predicted class (0 for land and 1 for water). All transfer functions are tan-sigmoids. The NN is trained with binary data (water or no water). The trained NN, however, when used in operational mode on new data, will provide a continuous value between 0 and 1 (Aires et al. 2017; Bishop 1995). This output represents the posterior probability to be one or the other class (Aires et al. 2017). The NN used here was developed with the Levenberg–Marquardt back-propagation algorithm over 7200 samples which were selected all over the plateau (with 50% water pixels and 50% nonwater pixels). Among them, 70% of samples were used for training, 15% for validation, and 15% for testing.

A step-forward approach was adopted in combination with the NN for the feature selection. Initially, six Landsat spectral bands were selected as the NN inputs, providing the basic information for classification. Then potential features, such as spectral index, topographic index, texture index, etc., were evaluated and selected one by one as input by calculating the mean square error (MSE) for the model's predictions. MSE provides a measure of how well the model's predictions align with the true values, with lower values indicating better performance. In each iteration, a potential feature is selected if its inclusion leads to a smaller MSE when combined with the previously selected features. This process is repeated until adding more features no longer results in a MSE improvement. Figure 8 shows the process of feature selection and the classification performance of each model over the testing database. The selected input features to the NN classifier were different for the four seasonal models, with 12 features selected for spring (6 surface reflectance bands plus DNMD, HAND, DNLD, TD, entropy, hue), 9 for summer (6 surface reflectance bands plus DNMD, HAND, slope), 12 for autumn (6 surface reflectance bands plus slope, NDVI, TD, DNLD, NDWI, mTPI), and 10 for winter (6 surface reflectance bands plus TD, DNMD, HAND, DNSD).

To test the performance of the seasonal models, the K-fold cross-validation method was used on each learning database (Kohavi 1995) (Fig. 9a). The original dataset is randomly and equally divided into K folds, and the model is trained K times, each time using $K - 1$ folds as the training data and the remaining fold as the testing data. The performance of the model is measured by calculating the average overall accuracy (number of correctly classified samples/total number of samples) and water accuracy (number of correctly classified samples for water/total number of water samples) across the K iterations. Here, K was assigned to 9 based on the number of months in which we collected samples for each model. The results show that each model had high overall classification and water accuracies, all above 95%. Also, the accuracy scores of the learning and testing datasets were close, indicating that the NN performed well in avoiding overfitting (i.e., performed well on the training dataset but generalized less well on unknown samples). The probability density function of the NN outputs also showed a clear distinction between water and nonwater for each model and also demonstrates that setting the threshold of 0.5 to binarize the classification outputs is reasonable (Fig. 9b). The stepwise forward selection (Fig. 8) was therefore efficient, and the selected seasonal NN architectures

Unauthenticated | Downloaded 01/16/25 10:26 AM UTC

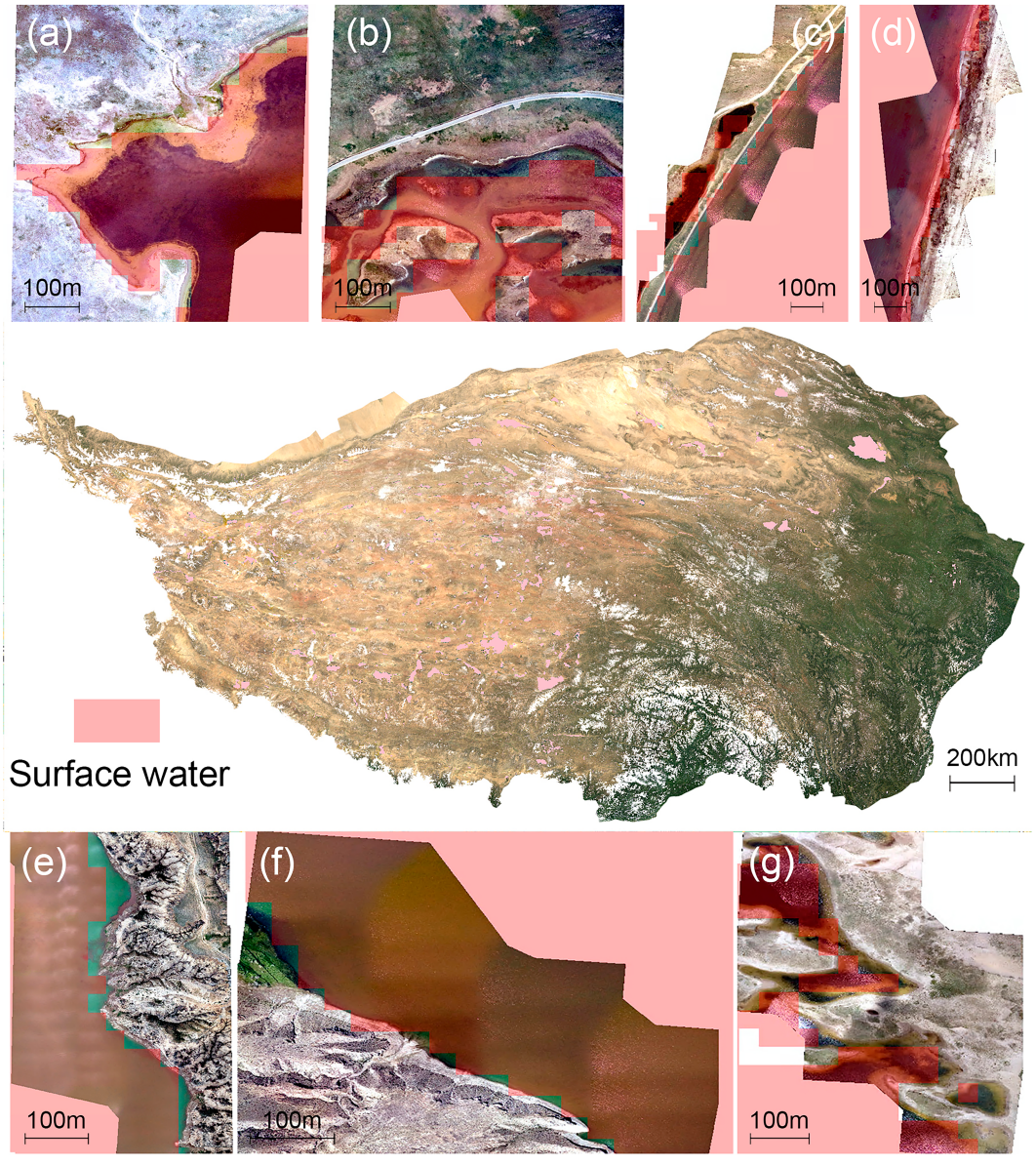

FIG. 10. Surface water classification result on the Qinghai–Tibet Plateau (shown in the middle row) and comparison of the UAV images and our classification result of (a)–(c) the Yellow River Sources, (d) the Qinghai Lake, (e),(f) the Longyang Gorge, and (g) the Star Lake in August 2020. Pink represents our classification result of surface water, which was overlayed on the Landsat images and UAV images.

that we used were sufficiently complex, but robust enough for the generalization skills of the predictions.

3) A POSTERIORI QUALITY FLAG

The output of the NN is between 0 and 1, denoting the probability of being classified as a target land-cover. The smaller the value of NN output, the greater the probability of being classified as a nonwater pixel. When the value is 0, the pixel can be labeled as nonwater without any ambiguity. On the contrary, the greater the value, the greater the probability of being classified as water. When the value is 1, the pixel can be labeled as water without any ambiguity. Here, we set a threshold of 0.5 to binarize the classification outputs. When the value is greater than 0.5, the pixel is labeled as water; otherwise, it is labeled as nonwater.

A quality flag (QF) was defined to measure the certainty that a pixel is correctly classified:

$$\mathrm{QF} = \begin{cases} |0 - \mathrm{nn}|, & \text{if } \mathrm{nn} < 0.5 \\ |1 - \mathrm{nn}|, & \text{if } \mathrm{nn} > 0.5 \end{cases},$$

where nn refers to the value of the nn output. The smaller the value of QF, the higher certainty of the classification result of the pixel is.

Unauthenticated | Downloaded 01/16/25 10:26 AM UTC

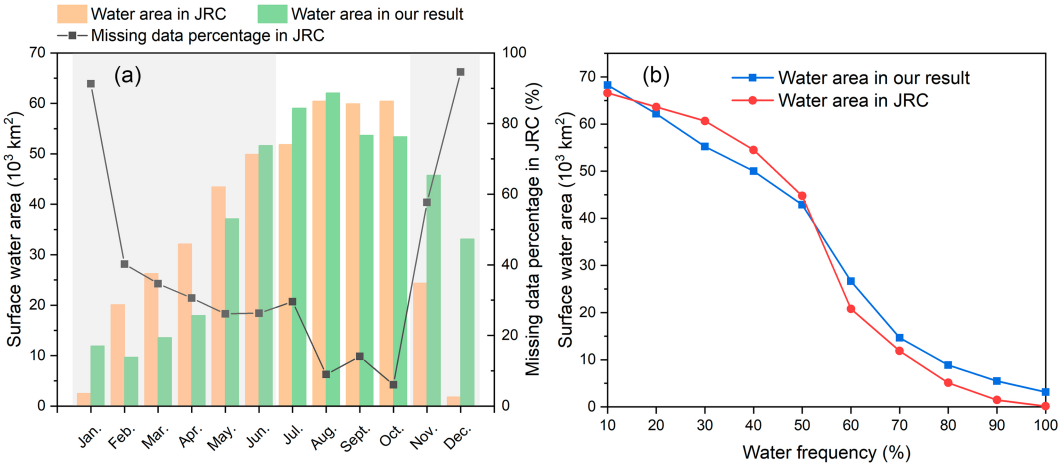

FIG. 11. (a) Comparison of monthly surface water area from JRC (orange bar) and from our results (green bar), the dark line refers to the percentage of missing data for JRC for each month of 2020, and gray shading indicates that the month is in the freezing period (Cai et al. 2019). (b) Variation of surface water area with water frequency in 2020 of JRC and our results.

d. Evaluation

Evaluation of our mapping result includes three processes: using independent validation samples, comparing the results on the water area and the spatial distribution with JRC mapping result, and evaluating with UAV images (for boundaries).

For the first part, independent validation samples consisted of ESA land-cover samples (section 2d), field samples (section 2d) and 15% independent samples from our sample database. The confusion matrix and several metrics were then calculated, including the overall accuracy, the user accuracy (U_Accuracy), the producer accuracy (P_Accuracy), and kappa coefficient. Here, the producer accuracy measures the accuracy of the model in correctly classifying water in the image, it is defined as the ratio of the number of correctly classified pixels of water to the total number of water pixels (Foody 2002). The user accuracy measures the accuracy of the model in representing the true land cover type on the ground as perceived by the user, it is defined as the ratio of the number of correctly classified pixels of water to the total number of pixels that the model classified as water (Foody 2002). The kappa coefficient is a statistical measure of interrater agreement or reliability for categorical data. The value of kappa ranges from −1 to 1, where 1 indicates perfect agreement, −1 indicates agreement worse than chance (Foody 2002). Then, our results on the water area and the spatial distribution were compared with the JRC monthly surface water maps. Finally, independent UAV images were used to validate our classification results.

4. Results and discussion

a. Evaluation of the surface water retrieval

1) EVALUATION WITH INDEPENDENT SAMPLES

Independent samples (field investigation, visual interpretation, and WorldCover dataset in Figs. 4 and 6) were used to evaluate the accuracy of both the JRC dataset and our results for August 2020 (Tables 4 and 5). Generally, the confusion matrix (Table 4) indicates that our results were highly consistent with independent reference data and achieved higher surface water mapping accuracy than the JRC dataset. The overall accuracy and kappa coefficient of our results (overall accuracy = 0.96, kappa = 0.90) were slightly higher than the JRC surface water map (overall accuracy = 0.94, kappa = 0.89). The producer accuracy of surface water in our results (0.94) was higher than in JRC (0.89), while the user accuracy of surface water in our results (0.98) was only slightly lower, compared with in JRC (0.99). The relatively lower producer accuracy compared with user accuracy indicated that there were omission errors for more than 100 water samples misclassified as nonwater (both in JRC and in our result). It may be related to the obscure water characteristics when these samples were located in small water bodies or under vegetation. Then, the accuracy of each land-cover type was calculated for further evaluation (Table 5). The higher water accuracy in our results (0.94) than in JRC (0.89) indicated that our results were more consistent with water samples, while JRC had a higher omission error of surface water. As for the nonwater surface types, especially for herbaceous wetland, our result had more commission errors, with lower accuracy (0.87) than JRC (0.99) in wetland classification. Wetland is defined as a transitional zone between aquatic systems and terrestrial where the land is sometimes covered by shallow water (Cowardin 1979). Therefore, there exist uncertainties in the wetland and water mapping. Further studies are needed to explore the relationships between water and wetlands. The classification accuracy was also assessed in specific regions where data interpolation was performed. The result shows that the water classification accuracy in this area reached 0.92 for August 2020, indicating a good performance of classification and the rationality of interpolation (appendix).

Unauthenticated | Downloaded 01/16/25 10:26 AM UTC

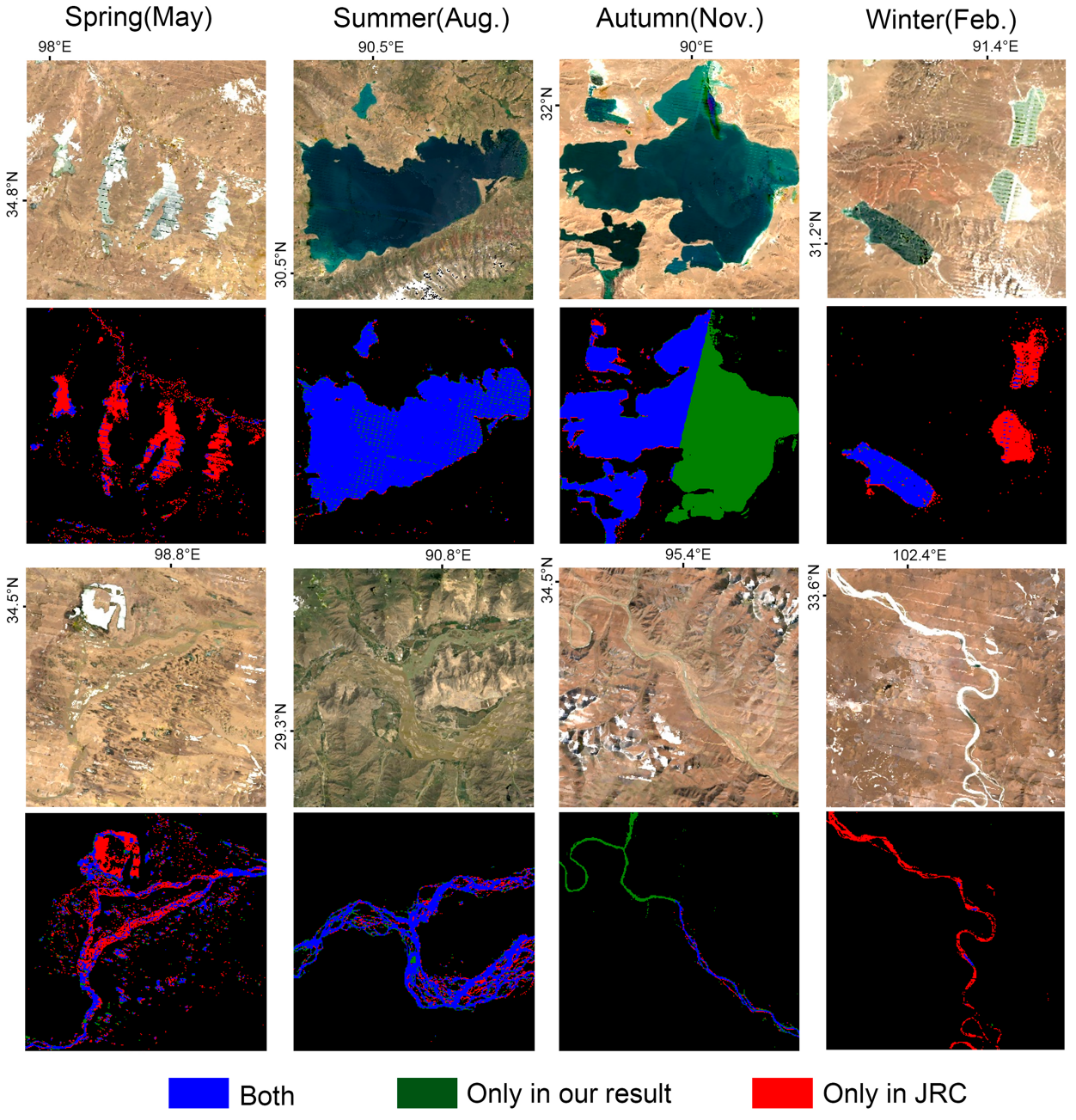

FIG. 12. Comparison of monthly surface water from JRC and from our results. Blue refers to pixels that were classified as water both in JRC and in our results, green represents pixels that were classified as water only in our results, and red represents pixels that were classified as water only in JRC.

2) VALIDATION WITH UAV IMAGES

UAV images were collected in the Yellow River sources (Figs. 10a–c), the Qinghai Lake (Fig. 10d), the Longyang Gorge (Figs. 10e,f), and the Star Lake (Fig. 10g) of the Qinghai–Tibet Plateau with a submeter spatial resolution. Generally, our results showed a clear delineation of the surface water boundary, as well as a precise detection of puddles (small water bodies) (Fig. 10). Figures 10b and 10e show a small part of omission errors, which may be caused by the mismatch of spatial resolution.

3) COMPARISON WITH JRC DATASET

Our results show that the monthly surface water fluctuated greatly in 2020, ranging from 9.701×10^3 km^2 (February) to 60.467×10^3 km^2 (August) (Fig. 11). Compared with JRC, there is no big difference with our classification result in the

Unauthenticated | Downloaded 01/16/25 10:26 AM UTC

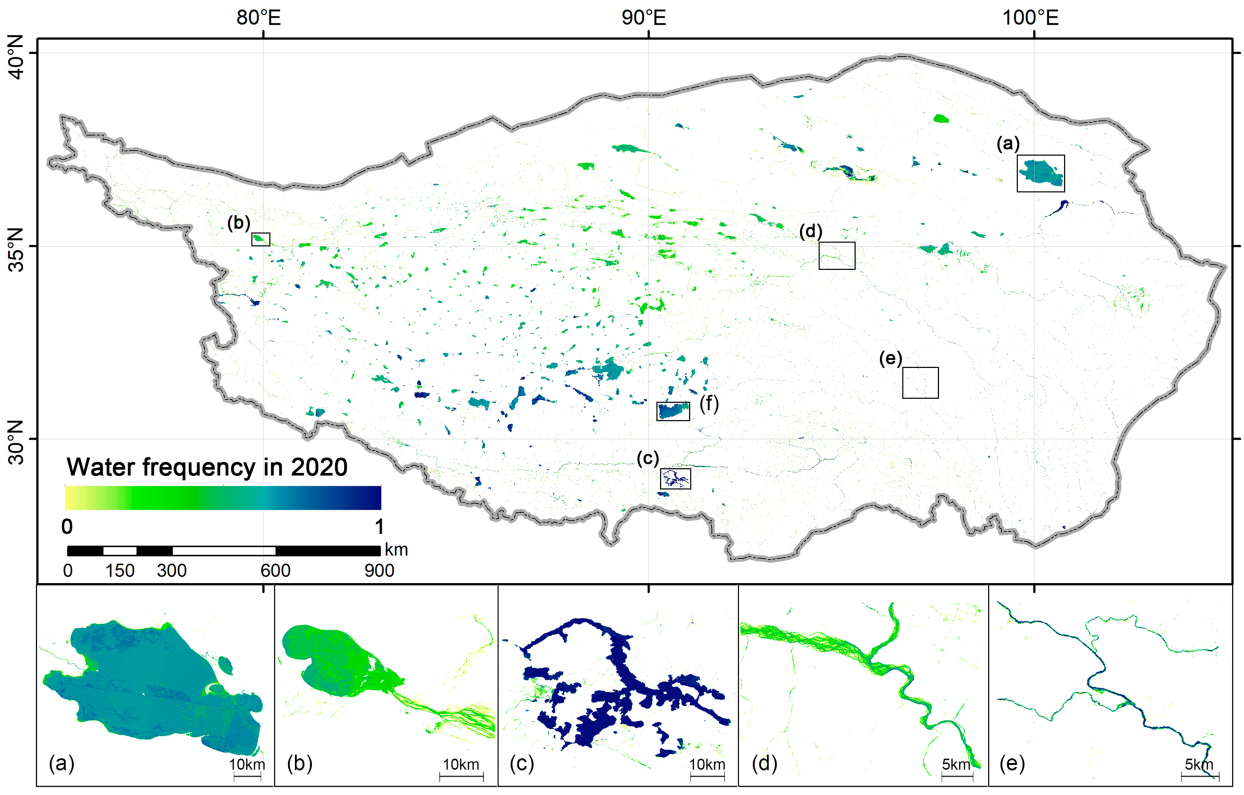

FIG. 13. Water frequency in 2020 in the Qinghai–Tibet Plateau.

summer period. However, the surface water areas of our results were much lower than that of JRC in spring (February–May), while much higher than the JRC in winter (November–January). The proportion of valid pixels in each month of the JRC dataset was counted, as shown with the black line in Fig. 11a. It can be seen that there existed a large amount of missing data in JRC, for example only three months (August, September, and October) had less than 10% missing data. The amount of missing data in January and December even reached over 90%. Thus, we suspected that the underestimation of the JRC dataset may be related to the existence of missing data (Meyer et al. 2020). The next section will provide a more detailed exploration of this. Water frequency is calculated by months with water divided by 12 months, which is always used as a criterion rule to define seasonal surface water and permanent surface water (Pickens et al. 2020; Yang et al. 2020). As shown in Fig. 11b, surface water areas with different water frequency thresholds differed between JRC and our results. When water frequency was smaller than 50%, the water areas were lower in our results than in JRC. When water frequency was larger than 50%, the water areas were larger in our results than in JRC. The overestimation and underestimation of surface water area affect the detection of water recurrence which is an important characteristic of water resources assessment and management (Mueller et al. 2016).

Figure 12 shows the classification results of the JRC and our study and the corresponding Landsat images. In summer, both of the JRC and our result had good performance on surface water extraction, but JRC slightly underestimated the water extent because it suffered from the missing data. It can be seen that the striped data gaps caused by sensors (Wang et al. 2012) in the JRC affect the spatial continuity of the large water bodies mapping, as the lake classification result in summer in Fig. 12. Also, there existed a large amount of data gaps in JRC as shown in November, so that only part of the lake and river have been detected. This problem may be related to cloud contamination (Zhang et al. 2017), and to the fact there are not enough images to cover all the region within a short time step after the cloud masking. The preprocessing in our study efficiently addressed this difficulty, and it is mandatory for monthly land information extraction studies. In freezing period (i.e., February and May), JRC seems to detect more water pixels than our results because the JRC classified erroneously ice cover as water. The overestimation of JRC in winter may be related to the decision tree–based classification procedure that may not be capable enough to separate water from ice/snow cover. The spectral indices of water and ice always have a nonnegligible overlap (Fig. 6). The high accuracy of water detection each month in our results indicate the stability and robustness of the seasonal classifier.

b. *Intra-annual variation of surface water in 2020*

In 2020, the maximum area of permanent surface water was 26.656×10^3 km^2, and the maximum area of permanent

Unauthenticated | Downloaded 01/16/25 10:26 AM UTC

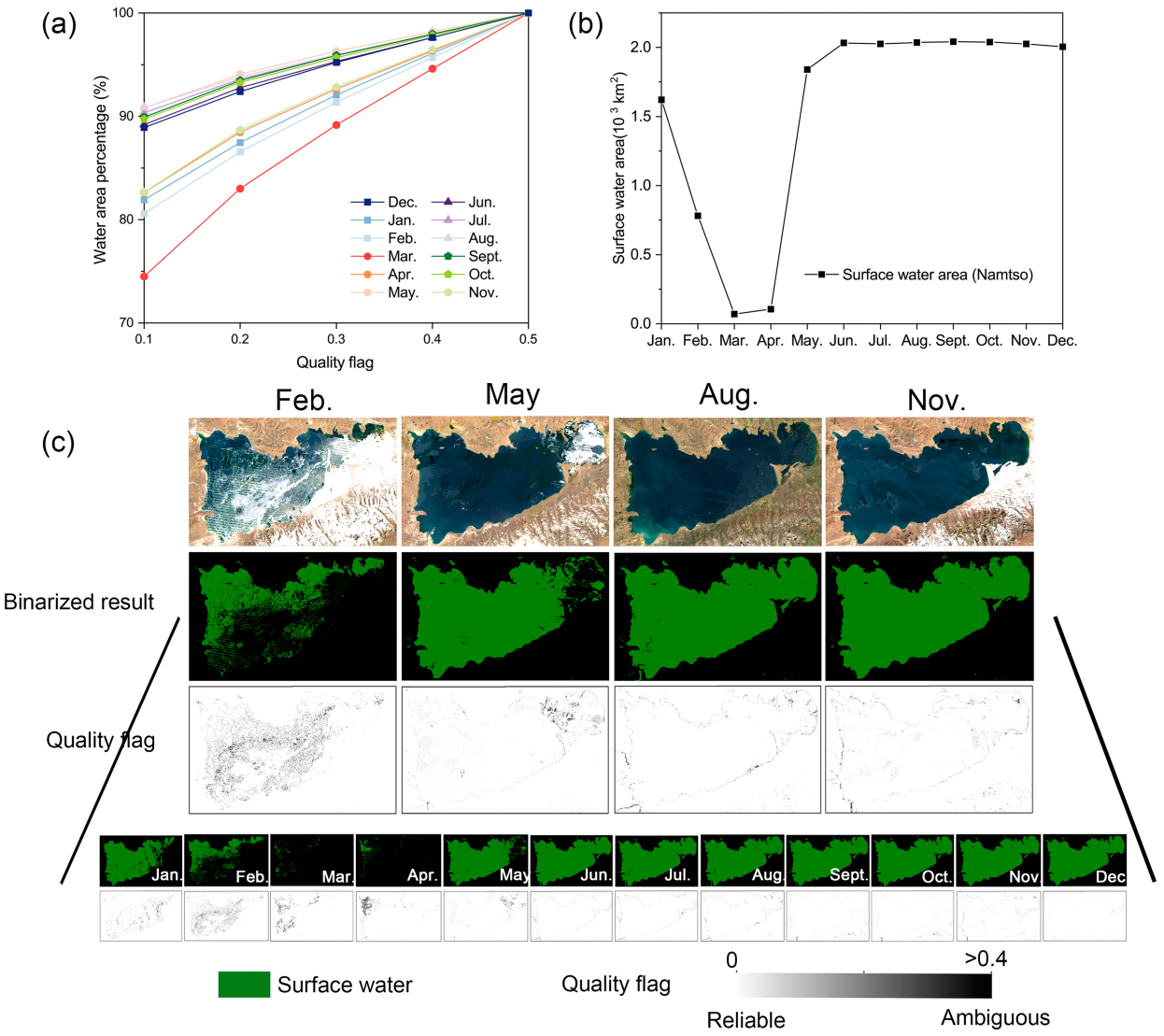

FIG. 14. (a) The surface water percentage under different quality flag levels in 2020 on the Qinghai–Tibet Plateau. The larger the quality flag, the higher certainty of the classification result. (b) Area variation of the monthly classification over Namtso (Fig. 13f). (c) Monthly water variations over Namtso. The top of the zoom shows the corresponding Landsat images, the second row is the classification result, and the third row is the quality flag. The bottom two rows are thumbnails of monthly classification results and quality flag images.

surface water and seasonal surface water was 55.246×10^3 km^2. In this study, we defined permanent surface water when water frequency is larger than 60%, considering the long ice cover period in the alpine ecosystem (Cai et al. 2019). Seasonal surface water was defined when water frequency was between 25% and 60%. Pixels with a water frequency lower than 25% were screened for the consideration of image quality, artifacts, etc. (Zou et al. 2018; Yang et al. 2020). The water recurrence is measured by the frequency with which water appears in a pixel (Li et al. 2021). It differs in regions and months in the Qinghai–Tibet Plateau, which is mainly related to the lake-ice phenology affected by water supply, geographical location, water physicochemical characteristics, and local climate condition (Cai et al. 2019, 2022; Guo et al. 2020).

Figure 13 shows the surface water frequency in 2020, with zoomed regions including lakes [Qinghai Lake (Fig. 13a), Aksai Chin Lake (Fig. 13b), Yamzho Yumco (Fig. 13c)] and rivers (Tongtian River and Jiqu Qu). In general, the water frequency was much smaller in the central and western Tibetan Plateau (Qiangtang Plateau) than in other regions. These results were consistent with Cai et al. (2019). The temperature and wind speed were lower in the central and western Tibetan Plateau, compared with the southern region, causing longer ice cover period with the earlier freeze-up dates and later breakup dates (Cai et al. 2019). Qinghai Lake, the largest saline inland lake in China, has moderate climate conditions and elevation on the plateau. Although the chemical properties of the salt lake lead to lower freezing points, the relatively

Unauthenticated | Downloaded 01/16/25 10:26 AM UTC

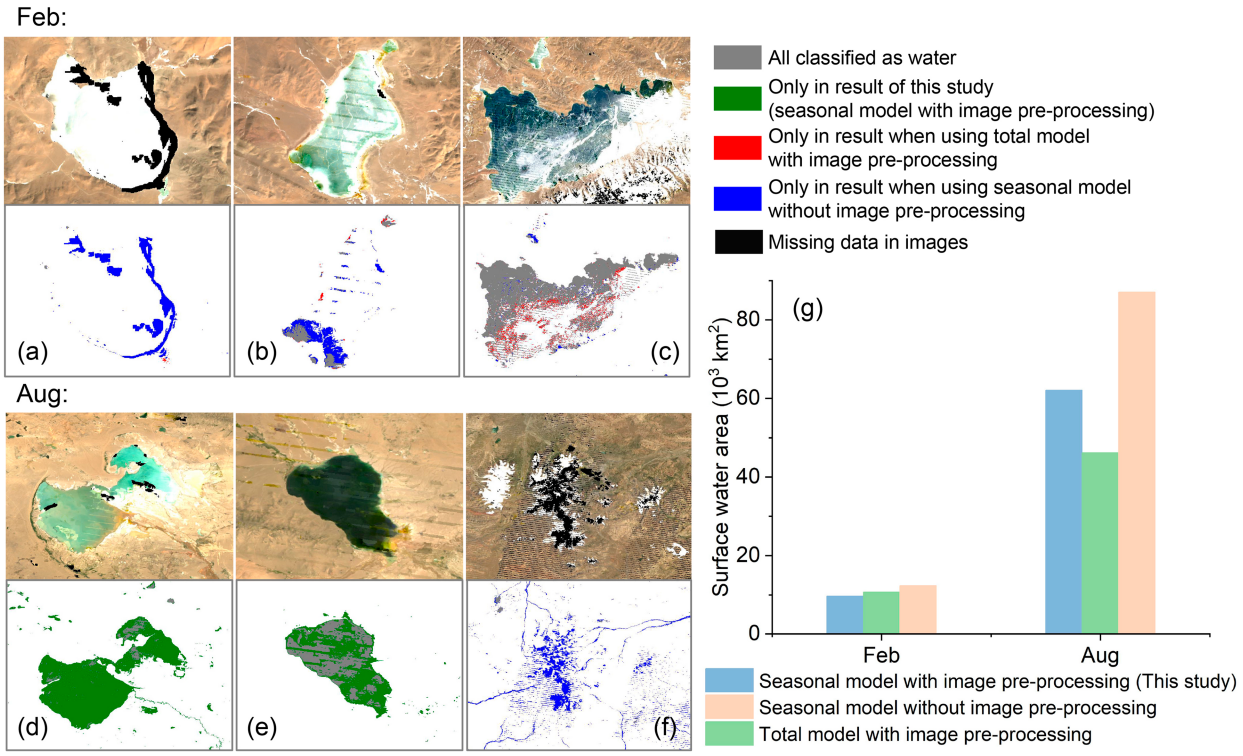

FIG. 15. (a)–(f) Comparison of surface water extent derived from three methods: the method proposed in this study using seasonal model with image preprocessing, the method using one total model with image preprocessing, and the method using a seasonal model without image preprocessing. The first row is the contemporaneous Landsat true color images. Black refers to missing data in images, gray refers to pixels that were classified as water in cases using three different methods, green refers to pixels that were classified as water only in this study, red refers to pixels that were classified as water only when using a total model, and blue refers to pixels that were classified as water when using seasonal model without image preprocessing. (g) The statistics of surface water area on the Qinghai–Tibet Plateau using the three different methods.

lower water frequency may be related to the lake size. Generally, a larger lake size implies larger volume, stronger vertical heat transfer, and less intense water evaporation, leading to a longer ice cover period (Yao et al. 2016).

Seasonal classification models for monthly water identification proved to be reasonable and efficient. Figure 14a represents the monthly QF statistics of the classification results for 2020. Figures 14b and 14c indicate the monthly surface water mapping results and QF of Namtso (Fig. 13f). Above 80% of the pixels had high certainty on the classification for each month (QF $<$ 0.2, Fig. 14a). Generally, the classification results of warmer months (July–September) had higher certainty than colder months (January–March). This further indicates that the surface water classification on the alpine ecosystem in the winter months is more likely to be confused with ice/snow cover and thus has higher uncertainties. In a typical region of Namtso, the delineation of the lake boundary was clear compared to land, while ambiguous regions mainly existed in the junction zone between the water body and the ice cover (Fig. 14c). For the lake-ice phenology, the lake started to freeze in January, froze completely in April, and melted in May. The areas of surface water in March and April were near 0, but they increased very fast from April to May. Surface water extent was maintained at high values (maximum of the distribution) from June to December (Figs. 14b,c).

c. *Strengths and prospects of surface water mapping framework*

The surface environmental features vary over time, such as vegetation coverage, water distribution, and snow and ice cover. By training models for different seasons, these land-cover differences can be better captured. The spectral index of surface water is prone to confusion with snow and ice cover (Fig. 6). Therefore, during the freezing period compared to open water bodies in summer, the model requires more information to obtain the distribution of water bodies (Fig. 8). In addition, the classification framework using seasonal neural network model with image preprocessing (dealing with invalid observation) showed better performance compared with two comparable methods: one using a total model with image preprocessing and the other using seasonal model without image preprocessing (Fig. 15). In February (the freezing period), methods using one total model or using seasonal model without image preprocessing were more inclined to identify ice/snow cover as water (Figs. 15b,c). In August (open water period), there existed lakes that were accurately delineated in

Unauthenticated | Downloaded 01/16/25 10:26 AM UTC

this study but were misclassified as nonwater when adopting one total model or adopting seasonal model without image preprocessing (Figs. 15d,e). Pixels with missing data were misclassified as water when using the method without image preprocessing (Figs. 15a,f). In terms of classification area, surface water area was overestimated in winter months when using one total model or using seasonal model without image preprocessing, and underestimation and overestimation both existed in summer months when adopting the other two comparable methods (Fig. 15g), which is consistent with our discussion above (Figs. 15a–f). Our method dealt with disturbance from the seasonal ice/snow cover during the freezing period and handled missing data more reasonably throughout the year, and the retrieval was more exploitable at the monthly scale.

Our method also showed several improvements over previous studies. First, the problem of invalid observations (e.g., missing and negative data) was solved at a finer temporal resolution, which guaranteed spatial continuity and greatly improved the accuracy of the classification result. Invalid observations are widespread in satellite images, especially in large-scale studies (Wang et al. 2012). The preprocessing was proved to be efficient for the average percentage improvement of monthly valid pixels, with an increased value from 86.3% to 99.7% (Fig. A1). Then, we trained seasonal models based on corresponding seasonal samples and a rigorous feature selection strategy (selection from 25 spectral and topographic features based on minimizing prediction MSE) to predict monthly images. Seasonal models showed a stable and robust performance for the monthly surface water mapping. Pekel et al. (2016) used a universal rule for monthly surface water detection, but the results showed many misclassifications in the winter months (Fig. 12). Xu et al. (2019) used seasonal/monthly training data and models to map seasonal/monthly cropland in three Landsat footprints and indicated a higher accuracy when using seasonal/monthly models. Considering the large scale and the complex land-cover conditions in the Qinghai–Tibet Plateau, different features were selected for each model in our study. Studies have shown that feature selection increased the classification accuracy and reduced the computation cost (Duro et al. 2012; Pal 2006). The characteristics of surface water (water depth, vegetation shade, etc.) and the other land cover types change greatly over time (Pickens et al. 2020), and the long ice cover period in the plateau (spanning autumn, winter, and spring) brings more uncertainties in the surface water detection (Cai et al. 2019; Ji et al. 2018). It is therefore necessary to specialize the learning database of different seasonal models. Third, the quality flag index was proposed for the first time to assess the pixel classification reliability. It revealed that above 80% of surface water had been extracted with a high confidence level, and uncertain or ambiguous classification results were mainly distributed in the junction of ice/snow cover and water in winter. Last but not least, the preliminary filtering of the potential water extent not only decreased the need for a large training sample size, but also reduced the classification data size and computation cost.

This study shows the great potential for application in monthly classification studies with high spatial resolution. An observation-based (in opposition to the present topography-based) floodability index could be obtained based on our monthly dataset (Nguyen and Aires 2023), which could provide precious information for future wetland mapping studies (Dvorett et al. 2016). Daily MODIS data with coarse-resolution data might be used with Landsat (16 days) images to capture a quick change of surface water (Aires et al. 2014). As optical/infrared satellite has limited penetration of the canopy, SAR data which are less sensitive to vegetation (Rao et al. 2019; White et al. 2015) could be introduced into the classification model. For the methodology, different types of neural network classifiers can be employed in the future. For example, using convolutional neural network models that take images as input can incorporate shape information and enable classification of different types of water bodies.

5. Conclusions

Surface water distribution changes extensively with time and space, and it is still a challenge to use remote sensing data for monthly surface water mapping with high spatial resolutions. This study proposed a robust NN-based monthly classification framework that precisely captured the monthly dynamics of surface water in the Qinghai–Tibet Plateau with accuracy. Our framework efficiently solved the problem of invalid observations and showed high performance in seasonal water and ice/snow cover separation in remote sensing images. The classification results showed higher accuracy than previous datasets, and they were highly consistent with the ground investigation and independent high-resolution images. The overall accuracy of surface water mapping reached 0.96 and more than 80% of the pixel classification results had a high-quality flag. This study shows the great potential for applications requiring monthly monitoring and high spatial resolution. In the future, a long time series monthly dataset and floodability index could be obtained based on this framework, which can provide precious information for wetland mapping studies, water resource management, and water security maintenance.

Acknowledgments. This work was financially supported by the Second Tibetan Plateau Scientific Expedition and Research (STEP) program (Grant 2019QZKK0304) and China Scholarship Council (CSC Grant 202004910673). We sincerely appreciate Yidi Xu for giving beneficial comments and are grateful to Hua Yu for the language revision. We are grateful to Boyang Ding, Zuopei Zhang, Hengli Lin, Yuzhen Xing, and Yang Chen from the University of Chinese Academy of Sciences and Donyu Dorjee, Pema Rigzin, Bianbaciren, Phuntsok Wangten, and Weihua Zhang from Tibet Meteorological Bureau, for providing the help of field investigation.

Data availability statement. The datasets used in this study, which consist of Landsat archive and topographic indices, are available from Google Earth Engine, GEE ID: IDAHO_EPSCOR/TERRACLIMATE, CSP/ERGo/1_0/Global, https://developers.google.com/earth-engine. The datasets generated in this study are available from https://data.tpdc.ac.cn/.

Unauthenticated | Downloaded 01/16/25 10:26 AM UTC

APPENDIX

Accuracy Assessment of the Interpolation Region

After the cloud masking, missing data were present every month over the Qinghai–Tibet Plateau (Fig. A1a). For instance, in July 2020, the worst month of that year, less than 70% of valid observations remained. Radiometric calibration also affects the reflection accuracy, resulting in negative reflectance values in some regions (Deng et al. 2018). Negative reflectance values in the monthly composite images were distributed over water and land (Fig. A1b). These negative values are invalid, making the derived spectral index value exceed the normal range, a true problem for the forthcoming classifier.

The number of images per month on a pixel scale after cloud masking and image fusion (*Landsat 7* and *Landsat 8*), indicating that approximately 80%, 68%, 72%, and 83% of the pixels contained two or more images in January, May, August, and November, respectively. To address data gaps, we performed interpolation based on a historical record.

Taking August 2020 as an example, the classification results for the specific regions were evaluated (interpolated data that were missing in the Landsat images). First, 200 water samples and 200 nonwater samples were randomly generated in this region according to our classification results (Fig. A2, August 2020). Then, these samples were checked by visual interpretation based on contemporaneous remote sensing images. Finally, the classification accuracy was calculated.

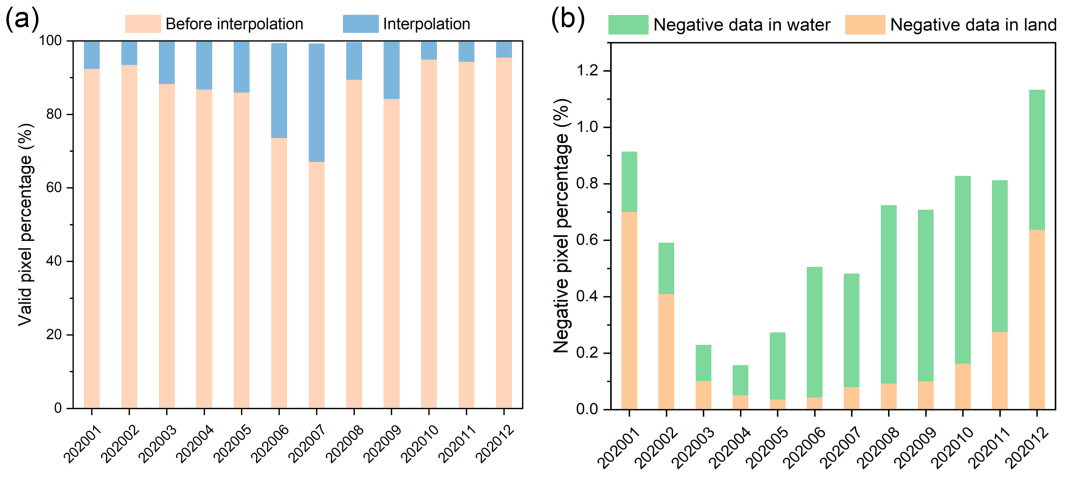

FIG. A1. (a) Percentage of valid Landsat pixels for each month of 2020 before (orange) and after (orange plus blue) the interpolation. (b) Percentage of negative data over land (orange) and water (green).

Unauthenticated | Downloaded 01/16/25 10:26 AM UTC

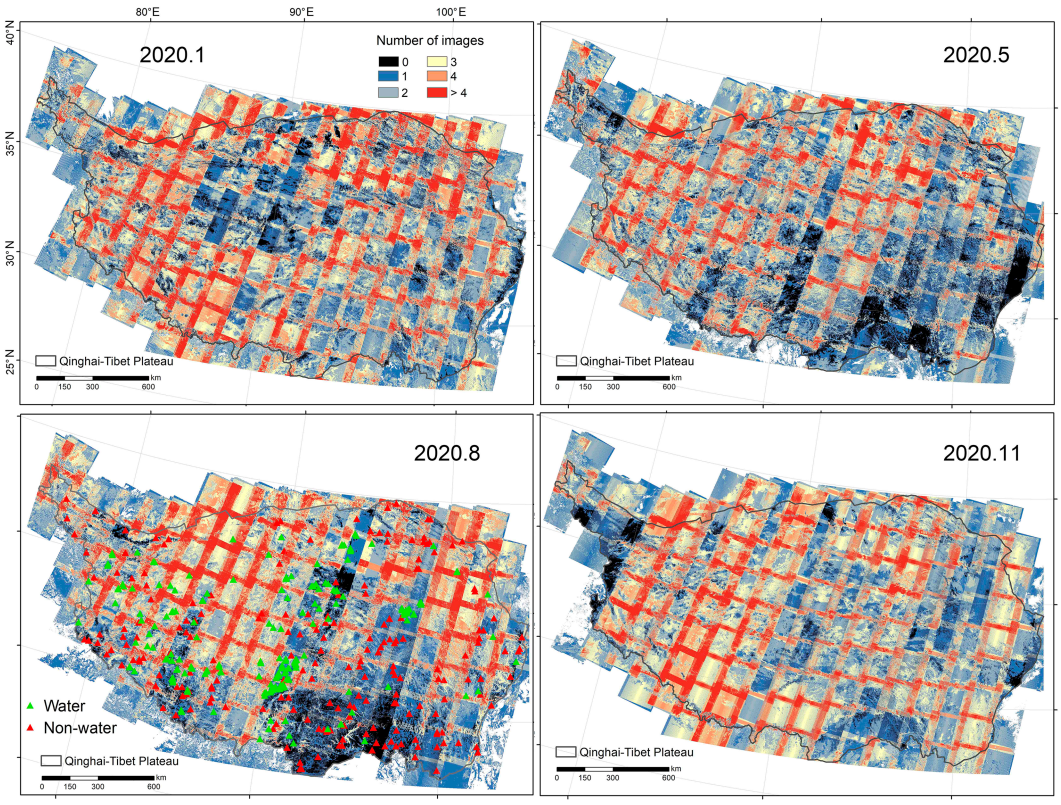

FIG. A2. The number of images on a pixel scale, in January, May, August, and November 2020. Validation samples were randomly generated over regions with missing data in August 2020.

REFERENCES

Aires, F., 2020: Surface water maps de-noising and missing-data filling using determinist spatial filters based on several a priori information. *Remote Sens. Environ.*, **237**, 111481, https://doi.org/10.1016/j.rse.2019.111481.

——, and V. Pellet, 2021: Estimating retrieval errors from neural network inversion schemes—Application to the retrieval of temperature profiles from IASI. *IEEE Trans. Geosci. Remote Sens.*, **59**, 6386–6396, https://doi.org/10.1109/TGRS.2020.3026944.

——, F. Papa, C. Prigent, J.-F. Crétaux, and M. Berge-Nguyen, 2014: Characterization and space–time downscaling of the inundation extent over the inner Niger Delta using GIEMS and MODIS data. *J. Hydrometeor.*, **15**, 171–192, https://doi.org/10.1175/JHM-D-13-032.1.

——, L. Miolane, C. Prigent, B. Pham, E. Fluet-Chouinard, B. Lehner, and F. Papa, 2017: A global dynamic long-term inundation extent dataset at high spatial resolution derived through downscaling of satellite observations. *J. Hydrometeor.*, **18**, 1305–1325, https://doi.org/10.1175/JHM-D-16-0155.1.

——, C. Prigent, E. Fluet-Chouinard, D. Yamazaki, F. Papa, and B. Lehner, 2018: Comparison of visible and multi-satellite global inundation datasets at high-spatial resolution. *Remote Sens. Environ.*, **216**, 427–441, https://doi.org/10.1016/j.rse.2018.06.015.

——, E. Boucher, and V. Pellet, 2021: Convolutional neural networks for satellite remote sensing at coarse resolution. Application for the SST retrieval using IASI. *Remote Sens. Environ.*, **263**, 112553, https://doi.org/10.1016/j.rse.2021.112553.

Bishop, C. M., 1995: *Neural Networks for Pattern Recognition*. Oxford University Press, 504 pp.

Bullock, E. L., C. E. Woodcock, and P. Olofsson, 2020: Monitoring tropical forest degradation using spectral unmixing and Landsat time series analysis. *Remote Sens. Environ.*, **238**, 110968, https://doi.org/10.1016/j.rse.2018.11.011.

Cai, Y., C.-Q. Ke, X. Li, G. Zhang, Z. Duan, and H. Lee, 2019: Variations of lake ice phenology on the Tibetan Plateau from 2001 to 2017 based on MODIS data. *J. Geophys. Res. Atmos.*, **124**, 825–843, https://doi.org/10.1029/2018JD028993.

——, ——, Y. Xiao, and J. Wu, 2022: What caused the spatial heterogeneity of lake ice phenology changes on the Tibetan Plateau? *Sci. Total Environ.*, **836**, 155517, https://doi.org/10.1016/j.scitotenv.2022.155517.

Chen, J., and Coauthors, 2017: 30-meter global land cover data product – GlobeLand30. Geomatics World, accessed 2021, www.globeland30.com.

Chen, Q., M. Huang, and X. Tang, 2020: Eutrophication assessment of seasonal urban lakes in China Yangtze River Basin using Landsat 8-derived Forel-Ule index: A six-year (2013–2018) observation. *Sci. Total Environ.*, **745**, 135392, https://doi.org/10.1016/j.scitotenv.2019.135392.

Conners, R. W., M. M. Trivedi, and C. A. Harlow, 1984: Segmentation of a high-resolution urban scene using texture operators. *Comput. Vision Graphics Image Process.*, **25**, 273–310, https://doi.org/10.1016/0734-189X(84)90197-X.

Unauthenticated | Downloaded 01/16/25 10:26 AM UTC

Cowardin, L. M., 1979: Classification of wetlands and deepwater habitats of the United States. Doc. FWS/OBS-79/31, Fish and Wildlife Service, U.S. Department of the Interior, 131 pp., https://www.fws.gov/wetlands/documents/classification-of-wetlands-and-deepwater-habitats-of-the-united-states.pdf.

Cybenko, G., 1989: Approximation by superpositions of a sigmoidal function. *Math. Control Signals Syst.*, **2**, 303–314, https://doi.org/10.1007/BF02551274.

Deng, L., Z. Mao, X. Li, Z. Hu, F. Duan, and Y. Yan, 2018: UAV-based multispectral remote sensing for precision agriculture: A comparison between different cameras. *ISPRS J. Photogramm. Remote Sens.*, **146**, 124–136, https://doi.org/10.1016/j.isprsjprs.2018.09.008.

Duro, D. C., S. E. Franklin, and M. G. Dubé, 2012: Multi-scale object-based image analysis and feature selection of multi-sensor Earth observation imagery using random forests. *Int. J. Remote Sens.*, **33**, 4502–4526, https://doi.org/10.1080/01431161.2011.649864.

Dvorett, D., C. Davis, and M. Papeş, 2016: Mapping and hydrologic attribution of temporary wetlands using recurrent Landsat imagery. *Wetlands*, **36**, 431–443, https://doi.org/10.1007/s13157-016-0752-9.

Feng, M., J. O. Sexton, S. Channan, and J. R. Townshend, 2016: A global, high-resolution (30-m) inland water body dataset for 2000: First results of a topographic-spectral classification algorithm. *Int. J. Digit. Earth*, **9**, 113–133, https://doi.org/10.1080/17538947.2015.1026420.

Feyisa, G. L., H. Meilby, R. Fensholt, and S. R. Proud, 2014: Automated water extraction index: A new technique for surface water mapping using Landsat imagery. *Remote Sens. Environ.*, **140**, 23–35, https://doi.org/10.1016/j.rse.2013.08.029.

Fisher, A., N. Flood, and T. Danaher, 2016: Comparing Landsat water index methods for automated water classification in eastern Australia. *Remote Sens. Environ.*, **175**, 167–182, https://doi.org/10.1016/j.rse.2015.12.055.

Foody, G. M., 2002: Status of land cover classification accuracy assessment. *Remote Sens. Environ.*, **80**, 185–201, https://doi.org/10.1016/S0034-4257(01)00295-4.

Gao, B., 1996: NDWI—A normalized difference water index for remote sensing of vegetation liquid water from space. *Remote Sens. Environ.*, **58**, 257–266, https://doi.org/10.1016/S0034-4257(96)00067-3.

Georganos, S., T. Grippa, S. Vanhuysse, M. Lennert, M. Shimoni, and E. Wolff, 2018: Very high resolution object-based land use–land cover urban classification using extreme gradient boosting. *IEEE Geosci. Remote Sens. Lett.*, **15**, 607–611, https://doi.org/10.1109/LGRS.2018.2803259.

Ghorbanian, A., M. Kakooei, M. Amani, S. Mahdavi, A. Mohammadzadeh, and M. Hasanlou, 2020: Improved land cover map of Iran using Sentinel imagery within Google Earth Engine and a novel automatic workflow for land cover classification using migrated training samples. *ISPRS J. Photogramm. Remote Sens.*, **167**, 276–288, https://doi.org/10.1016/j.isprsjprs.2020.07.013.

Gong, P., and Coauthors, 2013: Finer resolution observation and monitoring of global land cover: First mapping results with Landsat TM and ETM+ data. *Int. J. Remote Sens.*, **34**, 2607–2654, https://doi.org/10.1080/01431161.2012.748992.

Gorelick, N., M. Hancher, M. Dixon, S. Ilyushchenko, D. Thau, and R. Moore, 2017: Google Earth Engine: Planetary-scale geospatial analysis for everyone. *Remote Sens. Environ.*, **202**, 18–27, https://doi.org/10.1016/j.rse.2017.06.031.

Gumbricht, T., R. M. Roman-Cuesta, L. Verchot, M. Herold, F. Wittmann, E. Householder, N. Herold, and D. Murdiyarso, 2017: An expert system model for mapping tropical wetlands and peatlands reveals South America as the largest contributor. *Global Change Biol.*, **23**, 3581–3599, https://doi.org/10.1111/gcb.13689.

Guo, L., H. Zheng, Y. Wu, T. Zhang, M. Wen, L. Fan, and B. Zhang, 2020: Responses of lake ice phenology to climate change at Tibetan Plateau. *IEEE J. Sel. Top. Appl. Earth Obs. Remote Sens.*, **13**, 3856–3861, https://doi.org/10.1109/JSTARS.2020.3006270.

Halabisky, M., L. M. Moskal, A. Gillespie, and M. Hannam, 2016: Reconstructing semi-arid wetland surface water dynamics through spectral mixture analysis of a time series of Landsat satellite images (1984–2011). *Remote Sens. Environ.*, **177**, 171–183, https://doi.org/10.1016/j.rse.2016.02.040.

Hall, D. K., G. A. Riggs, and V. V. Salomonson, 1995: Development of methods for mapping global snow cover using moderate resolution imaging spectroradiometer data. *Remote Sens. Environ.*, **54**, 127–140, https://doi.org/10.1016/0034-4257(95)00137-P.

Haralick, R. M., K. Shanmugam, and I. Dinstein, 1973: Textural features for image classification. *IEEE Trans. Syst. Man Cybern.*, **6**, 610–621, https://doi.org/10.1109/TSMC.1973.4309314.

Ienco, D., R. Gaetano, C. Dupaquier, and P. Maurel, 2017: Land cover classification via multitemporal spatial data by deep recurrent neural networks. *IEEE Geosci. Remote Sens. Lett.*, **14**, 1685–1689, https://doi.org/10.1109/LGRS.2017.2728698.

Ji, L., P. Gong, J. Wang, J. Shi, and Z. Zhu, 2018: Construction of the 500-m resolution daily global surface water change database (2001–2016). *Water Resour. Res.*, **54**, 10 270–10 292, https://doi.org/10.1029/2018WR023060.

Jia, M., Z. Wang, D. Mao, C. Ren, C. Wang, and Y. Wang, 2021: Rapid, robust, and automated mapping of tidal flats in China using time series Sentinel-2 images and Google Earth Engine. *Remote Sens. Environ.*, **255**, 112285, https://doi.org/10.1016/j.rse.2021.112285.

Jiang, W., G. He, T. Long, Y. Ni, H. Liu, Y. Peng, K. Lv, and G. Wang, 2018: Multilayer perceptron neural network for surface water extraction in Landsat 8 OLI satellite images. *Remote Sens.*, **10**, 755, https://doi.org/10.3390/rs10050755.

Kohavi, R., 1995: A study of cross-validation and bootstrap for accuracy estimation and model selection. *Proc. 14th Int. Joint Conf. on Artificial Intelligence*, Montreal, QC, Canada, IJCAI, 1137–1145, https://www.ijcai.org/Proceedings/95-2/Papers/016.pdf.

Kordelas, G. A., I. Manakos, D. Aragonés, R. Díaz-Delgado, and J. Bustamante, 2018: Fast and automatic data-driven thresholding for inundation mapping with Sentinel-2 data. *Remote Sens.*, **10**, 910, https://doi.org/10.3390/rs10060910.

Kulkarni, A. D., and B. Lowe, 2016: Random forest algorithm for land cover classification. *Int. J. Recent Innovation Trends Comput. Commun.*, **4**, 58–63, https://doi.org/10.17762/ijritcc.v4i3.1834.

Li, X., and Coauthors, 2021: Monitoring high spatiotemporal water dynamics by fusing MODIS, Landsat, water occurrence data and DEM. *Remote Sens. Environ.*, **265**, 112680, https://doi.org/10.1016/j.rse.2021.112680.

Lu, S., and Coauthors, 2017: Lake water surface mapping in the Tibetan Plateau using the MODIS MOD09Q1 product. *Remote Sens. Lett.*, **8**, 224–233, https://doi.org/10.1080/2150704X.2016.1260178.

Meyer, M. F., S. G. Labou, A. N. Cramer, M. R. Brousil, and B. T. Luff, 2020: The global lake area, climate, and population

Unauthenticated | Downloaded 01/16/25 10:26 AM UTC

dataset. *Sci. Data*, **7**, 174, https://doi.org/10.1038/s41597-020-0517-4.

Mueller, N., and Coauthors, 2016: Water observations from space: Mapping surface water from 25 years of Landsat imagery across Australia. *Remote Sens. Environ.*, **174**, 341–352, https://doi.org/10.1016/j.rse.2015.11.003.

Nguyen, T.-H., and F. Aires, 2023: A global topography- and hydrography-based floodability index for the downscaling, analysis, and data-fusion of surface water. *J. Hydrol.*, **620**, 129406, https://doi.org/10.1016/j.jhydrol.2023.129406.

Pal, M., 2006: Support vector machine-based feature selection for land cover classification: A case study with DAIS hyperspectral data. *Int. J. Remote Sens.*, **27**, 2877–2894, https://doi.org/10.1080/01431160500242515.

——, and P. M. Mather, 2003: An assessment of the effectiveness of decision tree methods for land cover classification. *Remote Sens. Environ.*, **86**, 554–565, https://doi.org/10.1016/S0034-4257(03)00132-9.

Pekel, J.-F., A. Cottam, N. Gorelick, and A. S. Belward, 2016: High-resolution mapping of global surface water and its long-term changes. *Nature*, **540**, 418–422, https://doi.org/10.1038/nature20584.

Pickens, A. H., M. C. Hansen, M. Hancher, S. V. Stehman, A. Tyukavina, P. Potapov, B. Marroquin, and Z. Sherani, 2020: Mapping and sampling to characterize global inland water dynamics from 1999 to 2018 with full Landsat time-series. *Remote Sens. Environ.*, **243**, 111792, https://doi.org/10.1016/j.rse.2020.111792.

Qiao, C., J. Luo, Y. Sheng, Z. Shen, Z. Zhu, and D. Ming, 2012: An adaptive water extraction method from remote sensing image based on NDWI. *J. Indian Soc. Remote Sens.*, **40**, 421–433, https://doi.org/10.1007/s12524-011-0162-7.

Qu, B., Y. Zhang, S. Kang, and M. Sillanpää, 2019: Water quality in the Tibetan Plateau: Major ions and trace elements in rivers of the "Water Tower of Asia. *Sci. Total Environ.*, **649**, 571–581, https://doi.org/10.1016/j.scitotenv.2018.08.316.

Ran, Q., F. Aires, P. Ciais, C. Qiu, R. Hu, Z. Fu, K. Xue, and Y. Wang, 2023: The status and influencing factors of surface water dynamics on the Qinghai-Tibet Plateau during 2000–2020. *IEEE Trans. Geosci. Remote Sens.*, **61**, 1–14, https://doi.org/10.1109/TGRS.2022.3231552.

Rao, K., W. R. L. Anderegg, A. Sala, J. Martínez-Vilalta, and A. G. Konings, 2019: Satellite-based vegetation optical depth as an indicator of drought-driven tree mortality. *Remote Sens. Environ.*, **227**, 125–136, https://doi.org/10.1016/j.rse.2019.03.026.

Rezaee, M., M. Mahdianpari, Y. Zhang, and B. Salehi, 2018: Deep convolutional neural network for complex wetland classification using optical remote sensing imagery. *IEEE J. Sel. Top. Appl. Earth Obs. Remote Sens.*, **11**, 3030–3039, https://doi.org/10.1109/JSTARS.2018.2846178.

Rouse, J. W., R. H. Hass, J. A. Schell, D. W. Deering, and J. C. Harlan, 1974: Monitoring the vernal advancement and retrogradation (green wave effect) of natural vegetation. NASA Contractor Rep., 371 pp., https://ntrs.nasa.gov/citations/19750020419.

Scott, G. J., M. R. England, W. A. Starms, R. A. Marcum, and C. H. Davis, 2017: Training deep convolutional neural networks for land–cover classification of high-resolution imagery. *IEEE Geosci. Remote Sens. Lett.*, **14**, 549–553, https://doi.org/10.1109/LGRS.2017.2657778.

Senay, G. B., M. Schauer, M. Friedrichs, N. M. Velpuri, and R. K. Singh, 2017: Satellite-based water use dynamics using historical Landsat data (1984–2014) in the southwestern United States. *Remote Sens. Environ.*, **202**, 98–112, https://doi.org/10.1016/j.rse.2017.05.005.

Shen, H., H. Li, Y. Qian, L. Zhang, and Q. Yuan, 2014: An effective thin cloud removal procedure for visible remote sensing images. *ISPRS J. Photogramm. Remote Sens.*, **96**, 224–235, https://doi.org/10.1016/j.isprsjprs.2014.06.011.

Shen, M., 2011: Spring phenology was not consistently related to winter warming on the Tibetan Plateau. *Proc. Natl. Acad. Sci. USA*, **108**, E91–E92, https://doi.org/10.1073/pnas.1018390108.

Stefanov, W. L., M. S. Ramsey, and P. R. Christensen, 2001: Monitoring urban land cover change: An expert system approach to land cover classification of semiarid to arid urban centers. *Remote Sens. Environ.*, **77**, 173–185, https://doi.org/10.1016/S0034-4257(01)00204-8.

Tamiminia, H., B. Salehi, M. Mahdianpari, L. Quackenbush, S. Adeli, and B. Brisco, 2020: Google Earth Engine for geo-big data applications: A meta-analysis and systematic review. *ISPRS J. Photogramm. Remote Sens.*, **164**, 152–170, https://doi.org/10.1016/j.isprsjprs.2020.04.001.

Theobald, D. M., D. Harrison-Atlas, W. B. Monahan, and C. M. Albano, 2015: Ecologically-relevant maps of landforms and physiographic diversity for climate adaptation planning. *PLOS ONE*, **10**, e0143619, https://doi.org/10.1371/journal.pone.0143619.

Wang, G., D. Garcia, Y. Liu, R. de Jeu, and A. J. Dolman, 2012: A three-dimensional gap filling method for large geophysical datasets: Application to global satellite soil moisture observations. *Environ. Modell. Software*, **30**, 139–142, https://doi.org/10.1016/j.envsoft.2011.10.015.

Wang, X., and Coauthors, 2020: Gainers and losers of surface and terrestrial water resources in China during 1989–2016. *Nat. Commun.*, **11**, 3471, https://doi.org/10.1038/s41467-020-17103-w.

Wang, Z., J. Liu, J. Li, and D. D. Zhang, 2018: Multi-spectral water index (MuWI): A native 10-m multi-spectral water index for accurate water mapping on Sentinel-2. *Remote Sens.*, **10**, 1643, https://doi.org/10.3390/rs10101643.

White, L., B. Brisco, M. Dabboor, A. Schmitt, and A. Pratt, 2015: A collection of SAR methodologies for monitoring wetlands. *Remote Sens.*, **7**, 7615–7645, https://doi.org/10.3390/rs70607615.

Wu, S., H. Chen, Z. Zhao, H. Long, and C. Song, 2014: An improved remote sensing image classification based on *K*-means using HSV color feature. *10th Int. Conf. on Computational Intelligence and Security*, Los Alamitos, CA, Institute of Electrical and Electronics Engineers, 201–204, https://doi.ieeecomputersociety.org/10.1109/CIS.2014.90.

Wu, W., Y. Shi, K. Cai, K. Li, L. Cering, and Z. Gong, 2021: Using an explicit multi-feature decision tree for wetland information extraction in Qomolangma national nature reserve. *Remote Sens. Lett.*, **12**, 68–78, https://doi.org/10.1080/2150704X.2021.1875145.

Xu, H., 2006: Modification of normalised difference water index (NDWI) to enhance open water features in remotely sensed imagery. *Int. J. Remote Sens.*, **27**, 3025–3033, https://doi.org/10.1080/01431160600589179.

Xu, Y., and Coauthors, 2019: Exploring intra-annual variation in cropland classification accuracy using monthly, seasonal, and yearly sample set. *Int. J. Remote Sens.*, **40**, 8748–8763, https://doi.org/10.1080/01431161.2019.1620377.

Yamazaki, D., D. Ikeshima, J. Sosa, P. D. Bates, G. H. Allen, and T. M. Pavelsky, 2019: MERIT Hydro: A high-resolution global hydrography map based on latest topography dataset. *Water Resour. Res.*, **55**, 5053–5073, https://doi.org/10.1029/2019WR024873.

Unauthenticated | Downloaded 01/16/25 10:26 AM UTC

Yang, K., H. Wu, J. Qin, C. Lin, W. Tang, and Y. Chen, 2014: Recent climate changes over the Tibetan Plateau and their impacts on energy and water cycle: A review. *Global Planet. Change*, **112**, 79–91, https://doi.org/10.1016/j.gloplacha.2013.12.001.

Yang, X., Q. Qin, H. Yésou, T. Ledauphin, M. Koehl, P. Grussenmeyer, and Z. Zhu, 2020: Monthly estimation of the surface water extent in France at a 10-m resolution using Sentinel-2 data. *Remote Sens. Environ.*, **244**, 111803, https://doi.org/10.1016/j.rse.2020.111803.

Yao, X., L. Li, J. Zhao, M. Sun, J. Li, P. Gong, and L. An, 2016: Spatial-temporal variations of lake ice phenology in the Hoh Xil region from 2000 to 2011. *J. Geogr. Sci.*, **26**, 70–82, https://doi.org/10.1007/s11442-016-1255-6.

Zanaga, D., and Coauthors, 2021: ESA WorldCover 10 m 2020 v100. Zenodo, accessed 2021, https://doi.org/10.5281/zenodo.5571936.

Zhang, L., X. Li, Q. Yuan, and Y. Liu, 2014: Object-based approach to national land cover mapping using HJ satellite imagery. *J. Appl. Remote Sens.*, **8**, 083686, https://doi.org/10.1117/1.JRS.8.083686.

——, Q. Weng, and Z. Shao, 2017: An evaluation of monthly impervious surface dynamics by fusing Landsat and MODIS time series in the Pearl River Delta, China, from 2000 to 2015. *Remote Sens. Environ.*, **201**, 99–114, https://doi.org/10.1016/j.rse.2017.08.036.

Zhang, X., W. Shen, X. Zhuge, S. Yang, Y. Chen, Y. Wang, T. Chen, and S. Zhang, 2021: Statistical characteristics of mesoscale convective systems initiated over the Tibetan Plateau in summer by Fengyun satellite and precipitation estimates. *Remote Sens.*, **13**, 1652, https://doi.org/10.3390/rs13091652.

Zhu, X., F. Cai, J. Tian, and T. K.-A. Williams, 2018: Spatiotemporal fusion of multisource remote sensing data: Literature survey, taxonomy, principles, applications, and future directions. *Remote Sens.*, **10**, 527, https://doi.org/10.3390/rs10040527.

Zhu, Z., 2017: Change detection using Landsat time series: A review of frequencies, preprocessing, algorithms, and applications. *ISPRS J. Photogramm. Remote Sens.*, **130**, 370–384, https://doi.org/10.1016/j.isprsjprs.2017.06.013.

Zou, Z., J. Dong, M. A. Menarguez, X. Xiao, Y. Qin, R. B. Doughty, K. V. Hooker, and K. D. Hambright, 2017: Continued decrease of open surface water body area in Oklahoma during 1984–2015. *Sci. Total Environ.*, **595**, 451–460, https://doi.org/10.1016/j.scitotenv.2017.03.259.

——, X. Xiao, J. Dong, Y. Qin, R. B. Doughty, M. A. Menarguez, G. Zhang, and J. Wang, 2018: Divergent trends of open-surface water body area in the contiguous United States from 1984 to 2016. *Proc. Natl. Acad. Sci. USA*, **115**, 3810–3815, https://doi.org/10.1073/pnas.1719275115.

Unauthenticated | Downloaded 01/16/25 10:26 AM UTC